

1 **Coversheet for “Intraseasonal Sea-Level Variability in the**
2 **Persian Gulf”**

3 Christopher G. Piecuch^{1,†}, Ichiro Fukumori^{2,‡}, & Rui M. Ponte^{3,*}

4 ¹*Woods Hole Oceanographic Institution, Woods Hole, Massachusetts, USA*

5 ²*Jet Propulsion Laboratory, Pasadena, California, USA*

6 ³*Atmospheric and Environmental Research, Inc., Lexington, Massachusetts, USA*

7 This is a non-peer reviewed preprint submitted to Earth and Space Science Open Archive
8 (ESSOAr). This paper has been submitted to Journal of Physical Oceanography. Copyright in this
9 work may be transferred without further notice.

10 † cpiecuch@whoi.edu

11 ‡ ichiro.fukumori@jpl.nasa.gov

12 * rponte@aer.com

1 **Intraseasonal Sea-Level Variability in the Persian Gulf**

2 Christopher G. Piecuch*

3 *Woods Hole Oceanographic Institution, Woods Hole, Massachusetts, USA*

4 Ichiro Fukumori

5 *Jet Propulsion Laboratory, Pasadena, California, USA*

6 Rui M. Ponte

7 *Atmospheric and Environmental Research, Inc., Lexington, Massachusetts, USA*

8 *Corresponding author: Christopher G. Piecuch, cpiecuch@whoi.edu

ABSTRACT

9 Satellite observations are used to establish the dominant magnitudes, scales, and mechanisms
10 of intraseasonal variability in ocean dynamic sea level (ζ) in the Persian Gulf over 2002–2015.
11 Empirical orthogonal function (EOF) analysis applied to altimetry data reveals a basin-wide, single-
12 signed intraseasonal fluctuation that contributes importantly to ζ variance in the Persian Gulf at
13 monthly to decadal timescales. An EOF analysis of Gravity Recovery and Climate Experiment
14 (GRACE) observations over the same period returns a similar large-scale mode of intraseasonal
15 variability, suggesting that the basin-wide intraseasonal ζ variation has a predominantly barotropic
16 nature. A linear barotropic theory is developed to interpret the data. The theory represents
17 Persian-Gulf-average ζ ($\bar{\zeta}$) in terms of local freshwater flux, barometric pressure, and wind stress
18 forcing, as well as ζ at the boundary in the Gulf of Oman. The theory is tested using a multiple
19 linear regression with these freshwater flux, barometric pressure, wind stress, and boundary ζ
20 quantities as input, and $\bar{\zeta}$ as output. The regression explains $70\% \pm 9\%$ (95% confidence interval)
21 of the intraseasonal $\bar{\zeta}$ variance. Numerical values of regression coefficients computed empirically
22 from the data are consistent with theoretical expectations from the theory. Results point to a
23 substantial non-isostatic response to surface loading. The Gulf of Oman ζ boundary condition
24 shows lagged correlation with ζ upstream along the Indian Subcontinent, Maritime Continent,
25 and equatorial Indian Ocean, suggesting a large-scale Indian-Ocean influence on intraseasonal $\bar{\zeta}$
26 variation mediated by coastal and equatorial waves, and hinting at potential predictability. This
27 study highlights the value of GRACE for understanding sea level in an understudied marginal sea.

28 **1. Introduction**

29 The Persian Gulf¹ is a semi-enclosed marginal sea of the Indian Ocean (Figure 1). It connects to
30 the Arabian Sea to the southeast through the Strait of Hormuz and the Gulf of Oman. The Persian
31 Gulf is shallow and broad, with an average depth of ~ 30 m and a surface area of $\sim 2.2 \times 10^5$ km².
32 It is subject to an arid, subtropical climate, and is bounded to the southwest by the Arabian Desert
33 and by the Zagros mountains to the northeast.

34 Past studies establish the basic physical oceanography of the Persian Gulf using data and models
35 (Chao et al., 1992; Emery, 1956; Johns et al., 1999, 2003; Kämpf and Sadrinasab, 2006; Reynolds,
36 1993; Thoppil and Hogan, 2010; Swift and Bower, 2003; Yao and Johns, 2010). We outline some
37 of the salient features for context. The region is forced year-round by north-northwesterly surface
38 winds ('shamal', speeds 3–6 m s⁻¹). Evaporation (~ 2 m y⁻¹) far exceeds precipitation and runoff
39 (~ 0.2 m y⁻¹), resulting in an inverse-estuarine circulation—fresher, warmer buoyant waters inflow
40 near the surface through the Strait of Hormuz largely along the coast of Iran, whereas saltier, colder,
41 denser waters outflow near the bottom mainly along the coast of the United Arab Emirates. The
42 basin-scale circulation is demarcated by a thermal front across the Persian Gulf between Qatar and
43 Iran. Northwest of the front, there is equatorward flow along Saudi Arabia driven by wind-forced
44 downwelling at the coast and buoyant river discharge from the Tigris, Euphrates, and other rivers
45 at the head of the Persian Gulf. To the southeast, there exists a large-scale counterclockwise
46 circulation, maintained by exchanges through the Strait of Hormuz, and evaporation, cooling, and
47 sinking of water masses in shallow regions along the southern Persian Gulf. Mesoscale eddies are
48 common, especially during boreal summer, when they are shed from the Iranian Coastal Jet due to
49 baroclinic instability. For more details, interested readers are directed to the papers cited above.

¹The name of this body of water is subject to dispute. It is also known as the Arabian Gulf or the Gulf. We use the name Persian Gulf following the conventions of the International Hydrographic Organization and the United Nations.

50 The Persian Gulf is one of the world ocean's busiest waterways, due to its vast oil and gas stores,
51 which are of longstanding geopolitical, economic, and military interest (al-Chalabi, 2007; Barnes
52 and Myers Jaffe, 2006; Larson, 2007). Bordering eight nations, the Persian Gulf is also home to
53 large coastal populations and major coastal cities including Dubai, Abu Dhabi, and Doha, which
54 are exposed to risk of flooding and inundation related to sea-level change (Al-Jeneid et al., 2008;
55 Lafta et al., 2020). Kopp et al. (2014, 2017) project that mean sea level will rise by 44–108 cm
56 between 2000 and 2100 in Bahrain under the Representative Concentration Pathway 8.5 forcing
57 scenario (66% confidence). This would threaten ~ 10–15% (~ 80–100 km²) of Bahrain's surface
58 area (Al-Jeneid et al., 2008). Such numbers emphasize the importance of understanding sea-level
59 changes in the Persian Gulf. However, projections of mean sea-level rise on multidecadal and longer
60 timescales (Kopp et al., 2014, 2017) alone are insufficient to anticipate future coastal flood risk.
61 Also important are sea-level fluctuations at decadal and shorter periods, which can superimpose
62 on longer-term changes, temporarily ameliorating or exacerbating coastal risk (Burgos et al., 2018;
63 Dangendorf et al., 2016; Long et al., 2020; Ray and Foster, 2016; Sweet et al., 2017). This
64 motivates a detailed investigation of mean sea-level variation in the Persian Gulf on decadal and
65 shorter timescales—what are the dominant magnitudes, scales, and mechanisms?

66 Past studies on Persian Gulf mean sea level largely focus on seasonal cycles and decadal trends
67 (Al-Subhi, 2010; Alothman et al., 2014; Ayhan, 2020; Barzandeh et al., 2018; El-Gindy, 1991;
68 El-Gindy and Eid, 1997; Hassanzadeh et al., 2007; Hosseinibalam et al., 2007; Sharaf El Din,
69 1990; Siddig et al., 2019; Sultan et al., 1995a, 2000). Sultan et al. (1995a) consider monthly
70 relative sea level during 1980–1990 from two tide gauges on the Saudi Arabia coast. They find
71 that 80% of the overall monthly data variance is explained by the seasonal cycle, which has an
72 amplitude of ~ 10 cm and peaks in boreal summer. These authors argue that 75% of the seasonal
73 variance in sea level reflects an inverted-barometer response to a ~ 10-mb-amplitude seasonal cycle

74 in local surface air pressure, and that the remaining 25% of seasonal variance represents steric
75 variability owing to density fluctuations. Other studies targeting different regions, tide gauges, and
76 time periods confirm this basic result that inverted-barometer and steric effects make primary and
77 secondary contributions, respectively, to the large-scale seasonal cycle in Persian Gulf sea level,
78 but also suggest that local wind effects are important in some places (Al-Subhi, 2010; Barzandeh
79 et al., 2018; El-Gindy, 1991; El-Gindy and Eid, 1997; Hassanzadeh et al., 2007; Hosseinibalam et
80 al., 2007; Sharaf El Din, 1990; Sultan et al., 2000). Alothman et al. (2014) interrogate monthly
81 relative sea level over 1979–2007 based on 15 tide-gauge records from Bahrain, Saudi Arabia, and
82 Iran, along with measurements of vertical land motion from 6 Global Positioning System (GPS)
83 stations in Bahrain, Saudi Arabia, and Kuwait. They determine that regional relative sea level rose
84 by $2.2 \pm 0.5 \text{ mm y}^{-1}$ over that time. These authors find that one-third of the increase ($0.7 \pm 0.6 \text{ mm}$
85 y^{-1}) was due to crustal subsidence, possibly related to groundwater pumping and oil extraction
86 (Amin and Bankher, 1997), and the remaining two-thirds ($1.5 \pm 0.8 \text{ mm y}^{-1}$) was due to geocentric
87 sea-level changes. Sultan et al. (2000) calculate a more muted relative sea-level trend (1.7 mm
88 y^{-1}) based on 9 tide-gauge records from Saudi Arabia over 1980–1994, while Siddig et al. (2019)
89 estimate a larger geocentric sea-level trend ($3.6 \pm 0.4 \text{ mm y}^{-1}$) from altimetry data averaged over
90 the Persian Gulf during 1993–2018, consistent with reports of a global sea-level acceleration in
91 recent decades (Nerem et al., 2018; Dangendorf et al., 2019; Frederikse et al., 2020).

92 Omitted from past works on Persian Gulf mean sea level is exploration of nonseasonal sea-level
93 variation. This is an important omission, since nonseasonal variations in general, and in particular
94 intraseasonal variations, contribute importantly to mean sea-level variance over the Persian Gulf on
95 monthly to decadal timescales. For example, consider the time series of monthly ocean dynamic
96 sea level from satellite-altimetry data averaged over the Persian Gulf during 2002–2015 shown in
97 Figure 2. Filters are applied to the data to emphasize variability on different timescales, and global-

98 mean sea level and the inverted-barometer effect are removed. Nonseasonal fluctuations explain
99 52% of the monthly data variance, and intraseasonal fluctuations (with ~ 2 –6-month periods) alone
100 account for 46% of the overall data variance. The altimetric time series of intraseasonal sea level
101 averaged over the Persian Gulf also explains 51% of the intraseasonal variance in relative sea level
102 averaged across 5 tide gauges from Iran and Bahrain during the overlapping period 2002–2006
103 (Figure 2). This exploratory analysis suggests that large-scale intraseasonal fluctuations make
104 important contributions to ocean dynamic sea-level variance across the Persian Gulf during the
105 altimeter era, motivating a more in-depth investigation.

106 Here we investigate the magnitudes, scales, and mechanisms of intraseasonal sea-level variability
107 in the Persian Gulf through an analysis of satellite observations and other data. The remainder of
108 the paper is structured as follows: in section 2, we describe the data; in section 3, we establish
109 the horizontal scales and vertical structure of the dominant intraseasonal sea-level variation in the
110 Persian Gulf; in section 4, we use dynamical theory, linear regression, and correlation analysis
111 to identify the main local and nonlocal forcing mechanisms and ocean dynamics responsible for
112 driving intraseasonal variations in Persian Gulf sea level and their relation to large-scale circulation
113 and climate in the Indian Ocean; we conclude with a summary and discussion in section 5.

114 **2. Materials and Methods**

115 *a. Ocean dynamic sea level from satellite altimetry*

116 We use version 2.0 of the sea-level essential climate variable product from the European Space
117 Agency Climate Change Initiative (Legeais et al., 2018; Quartly et al., 2017). Data were down-
118 loaded from the Centre for Environmental Data Analysis on 18 April 2020. (All data sources are
119 indicated in Table 1.) The multi-satellite merged geocentric sea-level anomalies are given on a

120 0.25° global spatial grid and a monthly time increment during 1993–2015. These data extend and
121 update the earlier version 1.1 product (Ablain et al., 2015). The dynamic atmospheric correction
122 is applied, which involves removing the ocean’s dynamic barotropic response to wind and pressure
123 forcing at shorter periods < 20 days and its isostatic response to pressure forcing at longer periods
124 > 20 days from the data (Carrère and Lyard, 2003; Carrère et al. 2016). (The dynamic ocean
125 response to these forcings at the periods of interest to this study are retained in the data.) For
126 more details on the geophysical corrections, orbit solutions, altimeter standards, and error budgets,
127 see Quartly et al. (2017) and Legeais et al. (2018). We remove the time series of global-mean
128 geocentric sea-level values from every grid cell. Assuming that gravitational, rotational, and defor-
129 mational effects are negligible (Gregory et al., 2019), the resulting sea-level anomalies represent
130 ocean dynamic sea-level anomalies². We use the data from May 2002 to September 2015, since
131 this is the period of overlap between this altimeter data set and the Gravity Recovery and Climate
132 Experiment (GRACE), which is used for interpretation and described below. Following Gregory
133 et al. (2019), we use ζ to denote ocean dynamic sea level.

134 This paper focuses on intraseasonal variability. To isolate intraseasonal behavior, we process
135 the data as follows. We use least squares to estimate the seasonal cycle (annual and semi-annual
136 sinusoids) and linear trend in the data over the study period. We then remove these seasonal and
137 trend contributions from the original data to create a time series of nonseasonal residuals. Next, we
138 apply a Gaussian smoother with a 3-month half window to these nonseasonal residuals. Finally,
139 we subtract this low-pass-filtered time series from the nonseasonal residuals to create a record of
140 intraseasonal fluctuations, which is the object of our study. We delete the first and last 6 months of
141 the intraseasonal time series to avoid edge effects. This filter passes $> 90\%$ of the power at periods

²Ocean dynamic sea level refers to the local height of the sea surface above the geoid with the inverted-barometer correction applied (Gregory et al., 2019).

142 $\lesssim 8$ months and stops $> 70\%$ of the power at periods $\gtrsim 15$ months. See Figure 2 for an example of
143 this filtering applied to altimetry averaged over the Persian Gulf.

144 *b. Manometric sea level from satellite gravimetry*

145 We consider data from GRACE and GRACE Follow-On (Landerer et al., 2020; Watkins et al.,
146 2015; Wiese et al., 2016). Mass grids were downloaded from the National Aeronautics and Space
147 Administration Jet Propulsion Laboratory on 15 April 2020 (data version JPL RL06M.MSCNv02).
148 The data are processed using 3° spherical-cap mass-concentration blocks for the gravity-field basis
149 functions. For more details on the estimation process, spatial constraints, scale factors, and leakage
150 errors, see Watkins et al. (2015). The data are defined on a 0.5° global spatial grid, but the satellite
151 measurement do not resolve processes with spatial scales $\lesssim 300$ km. We use the version of the
152 data with the coastline resolution improvement filter applied (Wiese et al., 2016). The grids are
153 defined at irregular, quasi-monthly increments, and have gaps. For example, battery management
154 issues caused multi-month data gaps in the final years of GRACE, and there is a ~ 1 -y data gap
155 between the end of GRACE coverage and the beginning of the GRACE Follow-On record. We
156 linearly interpolate the available ocean mass grids onto regular monthly increments from May 2002
157 through September 2015. The data have units of equivalent water thickness. After correcting for
158 global air-pressure effects, these data reflect manometric sea-level anomalies³. To isolate dynamic
159 manometric sea-level anomalies associated with internal ocean mass redistribution, we subtract the
160 time series of barystatic sea level⁴ from the data at every oceanic grid cell. Intraseasonal variations
161 are isolated through filtering methods described earlier. Following Gregory et al. (2019), we use
162 R_m to indicate manometric sea level, with its dynamic nature understood.

³Manometric sea-level changes indicate sea-level changes due to changes in the local mass of the ocean per unit area (Gregory et al., 2019).

⁴Barystatic sea-level changes refer to global-mean sea-level changes due to net addition or subtraction of water mass to or from the global ocean (Gregory et al., 2019).

163 *c. Relative sea level from tide gauges*

164 We also use monthly mean relative sea level⁵ from tide-gauge records in the Persian Gulf that
165 overlap with our study period (Table 2). Data were downloaded from the Permanent Service for
166 Mean Sea Level database on 1 July 2019 (PSMSL, 2019; Holgate et al., 2013). The data from Mina
167 Sulman in Manama, Bahrain represent the only record from the Persian Gulf in the PSMSL database
168 with a complete benchmark datum history (so-called revised local reference data). To consider
169 large-scale regional behavior, we also study a careful selection of records without continuous datum
170 histories (so-called metric data). Namely, we use the data from Emam Hassan, Bushehr, Kangan,
171 and Shahid Rajaei in Iran⁶. We consider the data over 2002–2006, since earlier times predate
172 our study, and later times feature no tide-gauge data (Table 2). The data from Emam Hassan
173 before November 2002 are omitted due to a data gap that coincided with an apparent datum shift
174 (Allothman et al., 2014). We adjust each record for the inverted-barometer effect using reanalysis
175 surface air pressure (see below). Next, we remove the seasonal cycle and linear trend from each
176 adjusted time series. We then average together these nonseasonal time series to create a regional
177 composite of adjusted relative sea level. Finally, we isolate intraseasonal variability by computing
178 and then removing a low-pass-filtered version of the regional composite. The resulting time series
179 is shown in Figure 2. To the extent that global-mean sea-level changes and gravitational, rotational,
180 and deformational effects are unimportant on these scales, this composite time series represents
181 tide-gauge-based intraseasonal regional ζ variability.

⁵Relative sea level is the height of the sea surface relative to the solid Earth (Gregory et al., 2019).

⁶Metric data from other Persian Gulf locations are also available in the PSMSL database. However, we determined that these records were unsuitable for our analysis. Five records from the United Arab Emirates, Qatar, and Iraq are short and predate our study period. A dozen records from Saudi Arabia were operated by the Saudi Arabian Oil Company and situated on oil platforms, and are therefore potentially unstable.

182 *d. Surface forcing*

183 We use gridded observations, atmospheric reanalyses, and flux estimates to interpret the data
184 from altimetry, GRACE, and tide gauges. For all fields, we compute intraseasonal anomalies
185 during 2002–2015 from the available monthly values, as with the altimetry and GRACE.

186 We use monthly wind stress and barometric pressure from the European Centre for Medium Range
187 Weather Forecasts Reanalysis Interim (ERA-Interim; Dee et al., 2011). Fields were downloaded
188 from the Woods Hole Oceanographic Institution (WHOI) Community Storage Server on 7 January
189 2019. Values are defined on a 0.75° global spatial grid from January 1979 to October 2018.

190 We use monthly evaporation from version 3 of the the Objectively Analyzed air-sea Fluxes project
191 (OAFlux; Yu and Weller, 2007). Fields were downloaded from WHOI servers on 13 November
192 2019. Values are defined on a 1° global spatial grid from January 1958 to December 2018.

193 We use monthly precipitation from version 2.3 of the Global Precipitation Climatology Project
194 (GPCP; Adler et al., 2003). Fields were downloaded from National Oceanic and Atmospheric
195 Administration Earth System Research Laboratory and Physical Sciences Laboratory on 16 April
196 2020. Values are defined on a 2.5° global spatial grid from January 1979 to the present.

197 We use monthly river runoff from the Japanese 55-year atmospheric reanalysis surface data set
198 for driving ocean–sea-ice models (JRA55-do; Tsujino et al., 2018). Fields were downloaded from
199 servers at the Hokkaido University Graduate School of Environmental Science on 21 August 2020.
200 Values are defined on a 0.25° global coastal grid from January 1958 to December 2017.

201 **3. Horizontal scales and vertical structure of ζ variability**

202 Past studies use satellite altimetry and tide gauges to study seasonal cycles and decadal trends in
203 the Persian Gulf (Al-Subhi, 2010; Alothman et al., 2014; Ayhan, 2020; El-Gindy, 1991; El-Gindy
204 and Eid, 1997; Hassanzadeh et al., 2007; Hosseinibalam et al., 2007; Sharaf El Din, 1990; Siddig

205 et al., 2019; Sultan et al., 1995a, 2000). Here we examine intraseasonal variability in the Persian
206 Gulf using satellite data, including altimetry but also gravimetry, and tide gauges.

207 We motivated this study with an exploratory data analysis earlier in the introduction. We found
208 that roughly half of the monthly ζ variance from altimetry averaged over the Persian Gulf during
209 2002–2015 was concentrated at intraseasonal periods, and that the Persian-Gulf-average altimetric
210 time series of intraseasonal ζ ($\bar{\zeta}$) explained about half of the variance in a composite time series
211 of intraseasonal ζ from coastal tide gauges (Figure 2). These results show that intraseasonal
212 fluctuations contribute importantly to large-scale ζ variability over the Persian Gulf at monthly to
213 decadal periods, and that intraseasonal fluctuations measured locally at the coast largely reflect
214 spatially coherent, basin-wide behavior.

215 To explore intraseasonal ζ in more detail, we apply empirical orthogonal function (EOF) analysis
216 to altimetry data over the Persian Gulf. We identify the spatial structures and temporal behaviors of
217 the orthogonal modes of intraseasonal variability by solving for the eigenvalues and eigenvectors
218 of the covariance matrix of the altimetry data over the Persian Gulf. The eigenvectors correspond
219 to the spatial structures and the eigenvalues indicate the amounts of data variance explained by the
220 various modes. The temporal behaviors of the modes are described by principal-component time
221 series, which are determined by projecting the respective eigenvectors onto the data (von Storch
222 and Zwiers, 1999).

223 The leading mode, which explains 52% of the intraseasonal data variance over the Persian
224 Gulf, is summarized in Figures 3 and 4. It shows a single-signed spatial structure (Figure 3a),
225 indicating basin-wide variation and wholesale raising and lowering of ζ over the Persian Gulf.
226 This is consistent with our earlier finding that the $\bar{\zeta}$ time series from altimetry explains 51% of
227 the variance in the regional composite from tide gauges at intraseasonal timescales (Figure 2).
228 Indeed, this mode's principal-component time series (Figure 4) is perfectly correlated with the $\bar{\zeta}$

229 time series from altimetry (correlation coefficient > 0.99). The leading mode from a complex-
230 valued (Hilbert) EOF analysis explains the same amount of data variance (not shown). This means
231 that out-of-phase relationships between ζ in different parts of the Persian Gulf related to signal
232 propagation are unimportant to this mode, and that this dominant ζ variation reflects an in-phase
233 standing mode of oscillation across the region on these timescales.

234 The spatial structure is also nonuniform (Figure 3a). Magnitudes increase from southeast to
235 northwest across the region, with smaller values (1–3 cm) observed along the United Arab Emirates,
236 Qatar, Bahrain, and southern Iran, and larger values (3–5 cm) apparent off Saudi Arabia, Kuwait,
237 Iraq, and northern Iran. This basin-scale gradient could reflect wind setup related to strengthening
238 or weakening of the region’s prevailing north-northwesterlies. The strongest amplitudes (> 5 cm)
239 are detected off Kuwait and Iraq, near the mouths of the Tigris, Euphrates, and Karun rivers. Values
240 in this region are highest at the coast and decay offshore, possibly indicating trapped signals driven
241 by buoyant river discharge. There is also spatial structure in the amount of local data variance
242 explained by this mode: whereas 50–80% of local ζ data variance is explained over the interior
243 in the northwestern Persian Gulf, $< 30\%$ is explained in the southwest off Qatar, Bahrain, and
244 the United Arab Emirates (Figure 3b). This suggests important local-scale ζ variability along the
245 southwest coast that is unrelated to the broader-scale behavior resolved by this mode.

246 The ζ response to surface forcing is often described in terms of barotropic (depth-independent)
247 and baroclinic (depth-dependent) adjustments (e.g., Vinogradova et al., 2007). Given the latitude
248 of the Persian Gulf, and the spatiotemporal scales under investigation, basic scaling arguments
249 (Gill and Niiler, 1973; Piecuch et al., 2019) suggest that this mode of ζ variation should be
250 essentially barotropic in nature. For a purely barotropic ocean response, changes in sea level (or
251 subsurface pressure) are mirrored by changes in ocean bottom pressure (Bingham and Hughes,
252 2008; Vinogradova et al., 2007). Hence, if the leading mode of ζ variability from altimetry

253 (Figure 3, 4) reflects a predominantly barotropic response, then similar R_m variability should be
254 apparent in GRACE.

255 To test this hypothesis, we apply EOF analysis to the GRACE R_m grids over the Persian Gulf.
256 The results are shown in Figures 4 and 5. The leading mode, which explains 88% of the intrasea-
257 sonal GRACE data variance in the Persian Gulf, shows a single-signed spatial pattern, such that
258 variability increases from 1–2 cm in the southeastern Persian Gulf to 3–4 cm in the northwest
259 (Figure 5a). Relatively more local R_m data variance is explained ($> 80\%$) to the north and west,
260 while comparatively less is explained (50–70%) in the southeast (Figure 5b). These patterns from
261 GRACE are qualitatively similar to those from altimetry, but there are quantitative differences
262 (cf. Figures 3, 5). For example, the mode from altimetry exhibits larger amplitudes and richer,
263 more detailed spatial structures than the mode from GRACE (Figures 3a, 5a), whereas the leading
264 GRACE mode explains relatively more data variance compared to the leading altimetry mode
265 (Figures 3b, 5b). These discrepancies probably partly reflect the coarser resolution (and reduced
266 effective spatial degrees of freedom) of GRACE, but could also indicate baroclinic processes or
267 data errors (e.g., residual leakage of terrestrial signals into the GRACE ocean grids).

268 Such differences notwithstanding, results in Figures 3 and 5 suggest that GRACE and altime-
269 try capture facets of the same underlying mode of intraseasonal variation. This suggestion is
270 corroborated by the principal components of the leading EOF modes determined from GRACE
271 and altimetry, which are highly correlated (correlation coefficient of ~ 0.7 ; Figure 4). We also
272 apply maximum covariance analysis (MCA) jointly to altimetry ζ and GRACE R_m data, whereby
273 the eigenvalues and eigenvectors of the cross-covariance matrix between the two data sets are
274 determined (von Storch and Zwiers, 1999). The leading eigenvectors and principal components
275 determined jointly through MCA are identical to those determined separately through EOF anal-
276 ysis, and the gravest MCA mode explains $> 99\%$ of the joint covariance between altimetry and

277 GRACE data (not shown). This suggests that the leading modes of regional ζ and R_m variation are
 278 coupled to one another, and reflect a dominant barotropic response.

279 **4. Forcing mechanisms and ocean dynamics**

280 In the previous section, we established a basin-wide barotropic variation of the Persian Gulf on
 281 intraseasonal timescales. Here we use analytical theory, linear regression, and correlation analysis
 282 to identify the forcing and dynamics responsible for this mode.

283 *a. Linear barotropic model*

284 The leading mode of intraseasonal variability identified previously exhibits higher-order spatial
 285 structure (Figures 3, 5). However, the lowest-order spatial feature is that of a horizontally uniform
 286 fluctuation. For example, the time series of intraseasonal $\bar{\zeta}$ from altimetry explains 93% of the
 287 variance associated with the first altimetric EOF mode (Figures 2–4). Thus, we formulate a linear
 288 model for a horizontally uniform barotropic variation of the Persian Gulf. Our formulation largely
 289 follows Volkov et al. (2016), who use a similar model to consider ζ in the Black Sea. The equations
 290 for conservation of volume within the Persian Gulf and conservation of momentum along the Strait
 291 of Hormuz are

$$292 \quad S\bar{\zeta}_t = S\bar{q} + \frac{S}{\rho g}\bar{p}_t + vWH, \quad (1)$$

$$v_t = -g\zeta_y + \frac{1}{\rho H}\tau - \frac{r}{H}v. \quad (2)$$

293 Here S is surface area of the Persian Gulf, overbar is spatial average over the Persian Gulf, q is
 294 precipitation plus runoff minus evaporation, p is barometric pressure, v is average velocity along
 295 the Strait of Hormuz into the Persian Gulf (positive values increase the volume of the Persian Gulf),
 296 W and H are the width and depth of the Strait of Hormuz, respectively, τ is wind stress along the
 297 Strait of Hormuz (positive in the direction of the Persian Gulf), r is a constant friction coefficient,

298 g is gravity, ρ is seawater density, and subscripts t and y denote partial differentiation in time and
 299 the along-strait direction, respectively. Note that, since we express Eqs. (1) and (2) in terms of ζ ,
 300 forcing by p appears in the continuity equation rather than in the momentum equation, and takes
 301 on an analogous form to the q forcing, such that, as noted by Gill (1982), forcing by a depression
 302 of 10 mb would be canceled out by 10 cm of precipitation (cf. also Ponte, 2006). All symbols are
 303 described in Table 3 and representative values are given when appropriate.

304 We assume ζ , v , q , p , and τ take wave solutions of the form $\exp(-i\omega t)$ with angular frequency
 305 ω and $i \doteq \sqrt{-1}$. Integrating the momentum equation over the length L of the Strait of Hormuz, and
 306 rearranging to solve for $\bar{\zeta}$ gives

$$\bar{\zeta} = \left[\zeta_0 + \frac{L}{\rho g H} \tau + \frac{(\lambda - i\omega)}{\sigma^2} \bar{q} - i\omega \frac{(\lambda - i\omega)}{\sigma^2} \frac{\bar{p}}{\rho g} \right] \left/ \left[1 - \frac{\omega^2}{\sigma^2} - i \frac{\lambda \omega}{\sigma^2} \right], \quad (3)$$

307 where ζ_0 represents ζ at the boundary outside the Strait of Hormuz in the Gulf of Oman, and
 308 we define $\sigma^2 \doteq WHg/SL$ and $\lambda \doteq r/H$. Physically, $1/\lambda$ is a friction timescale and $1/\sigma$ is a
 309 Helmholtz resonance timescale determined by the shape of the Persian Gulf and Strait of Hormuz.
 310 (We determine that $1/\sigma \approx 15$ hours, which is small compared to the intraseasonal timescales of
 311 interest, so we do not expect a resonant response.) Equivalently, we can write Eq. (3) in the polar
 312 complex plane as

$$\bar{\zeta} = z_{\zeta_0} \exp(i\theta_{\zeta_0}) \zeta_0 + z_{\tau} \exp(i\theta_{\tau}) \tau + z_{\bar{q}} \exp(i\theta_{\bar{q}}) \bar{q} + z_{\bar{p}} \exp(i\theta_{\bar{p}}) \bar{p}, \quad (4)$$

313 where

$$\theta_{\zeta_0} \doteq \arctan\left(\frac{\lambda\omega}{\sigma^2 - \omega^2}\right), \quad (5)$$

$$z_{\zeta_0} \doteq \left[\left(1 - \frac{\omega^2}{\sigma^2}\right)^2 + \left(\frac{\lambda\omega}{\sigma^2}\right)^2 \right]^{-1/2}, \quad (6)$$

$$\theta_{\tau} \doteq \arctan\left(\frac{\lambda\omega}{\sigma^2 - \omega^2}\right), \quad (7)$$

$$z_\tau \doteq \left[\left(1 - \frac{\omega^2}{\sigma^2} \right)^2 + \left(\frac{\lambda\omega}{\sigma^2} \right)^2 \right]^{-1/2} \left(\frac{L}{\rho g H} \right), \quad (8)$$

$$\theta_{\bar{q}} \doteq \arctan \left(\frac{\lambda\omega}{\sigma^2} - \frac{\omega}{\lambda} + \frac{\omega^3}{\sigma^2\lambda} \right), \quad (9)$$

$$z_{\bar{q}} \doteq \frac{\lambda}{\sigma^2} \left[1 + \left(\frac{\lambda\omega}{\sigma^2} - \frac{\omega}{\lambda} + \frac{\omega^3}{\sigma^2\lambda} \right)^2 \right]^{1/2} \left[\left(1 - \frac{\omega^2}{\sigma^2} \right)^2 + \left(\frac{\lambda\omega}{\sigma^2} \right)^2 \right]^{-1}, \quad (10)$$

$$\theta_{\bar{p}} \doteq \arctan \left[\left(\frac{\omega}{\lambda} - \frac{\omega^3}{\lambda\sigma^2} - \frac{\omega\lambda}{\sigma^2} \right)^{-1} \right], \quad (11)$$

$$z_{\bar{p}} \doteq \frac{1}{\rho g} \frac{\lambda\omega}{\sigma^2} \left[1 + \left(\frac{\omega}{\lambda} - \frac{\lambda\omega}{\sigma^2} - \frac{\omega^3}{\sigma^2\lambda} \right)^2 \right]^{1/2} \left[\left(1 - \frac{\omega^2}{\sigma^2} \right)^2 + \left(\frac{\omega\lambda}{\sigma^2} \right)^2 \right]^{-1}, \quad (12)$$

In other words, according to Eq. (4), $\bar{\zeta}$ is a linear superposition of the ζ_0 , τ , \bar{q} , and \bar{p} forcing terms, each scaled by an amount z_j and rotated through a phase θ_j , where $j \in \{\zeta_0, \tau, \bar{q}, \bar{p}\}$. We estimate theoretical values for the scaling factors z_j and phase angles θ_j by averaging Eqs. (5)–(12) over the ω range from $2\pi / (6 \text{ months})$ to $2\pi / (2 \text{ months})$ using numerical values for the scalar coefficients λ , σ , L , ρ , g , and H from Table 3. These theoretical values are tabulated in Table 4.

b. Multiple linear regression analysis

To test whether the model described by Eqs. (1)–(12) is informative for understanding observed intraseasonal $\bar{\zeta}$ variability, we perform a multiple linear regression. We model $\bar{\zeta}$ from altimetry as

$$\bar{\zeta} = a_{\zeta_0}\zeta_0 + b_{\zeta_0}\mathcal{H}(\zeta_0) + a_\tau\tau + b_\tau\mathcal{H}(\tau) + a_{\bar{q}}\bar{q} + b_{\bar{q}}\mathcal{H}(\bar{q}) + a_{\bar{p}}\bar{p} + b_{\bar{p}}\mathcal{H}(\bar{p}) + \varepsilon, \quad (13)$$

where \mathcal{H} is the Hilbert transform, the a_j and b_j are real constants, and ε is the residual. We include Hilbert transforms of the various forcings in the regression to allow for possible phase lags between the forcing and the response, as indicated by Eq. (4). We estimate the z_j and θ_j from Eq. (4) from the a_j and b_j in Eq. (13) using properties of Hilbert transforms and trigonometric identities as

$$\theta_j = \arctan(b_j/a_j), \quad (14)$$

$$z_j = \sqrt{a_j^2 + b_j^2}. \quad (15)$$

334 We evaluate Eq. (13) using least squares. For ζ_0 , we use ζ from altimetry averaged over
 335 shallow regions (< 200 m) of the northern Gulf of Oman outside the Strait of Hormuz ($57\text{--}60^\circ\text{E}$,
 336 $25\text{--}28^\circ\text{N}$). For τ , we use along-strait wind stress (315°T) from ERA-Interim averaged over the
 337 Strait of Hormuz ($54\text{--}57.8^\circ\text{E}$, $22.9\text{--}27.4^\circ\text{N}$). For \bar{q} , we use precipitation from GPCP plus river
 338 runoff from JRA55-do minus evaporation from OAFflux averaged over the Persian Gulf ($45\text{--}55^\circ\text{E}$,
 339 $24\text{--}32^\circ\text{N}$). For \bar{p} , we use barometric pressure from ERA-Interim averaged over the Persian Gulf
 340 ($48\text{--}54.8^\circ\text{E}$, $24.4\text{--}29.6^\circ\text{N}$). Uncertainties are estimated using 10 000 iterations of bootstrapping
 341 (Efron and Hastie, 2016).

342 Results of the multiple linear regression are summarized in Figure 6. The regression model
 343 [(13)] explains $70\% \pm 9\%$ (95% confidence interval) of the variance in the $\bar{\zeta}$ data (Figure 6a). This
 344 suggests that Eqs. (1) and (2) represent the dominant physics, and that $\bar{\zeta}$ variability can be largely
 345 understood in terms of local surface forcing by τ , \bar{q} , and \bar{p} and nonlocal boundary forcing by ζ_0 .
 346 In Figure 6b, we break down the relative contributions of the different forcing terms. The primary
 347 driver of $\bar{\zeta}$ is nonlocal forcing by ζ_0 , which explains $50\% \pm 12\%$ of the $\bar{\zeta}$ variance. Local forcing
 348 by τ , \bar{q} , and \bar{p} plays a secondary role. Individually, τ explains $16\% \pm 9\%$, \bar{q} explains $5\% \pm 9\%$,
 349 and \bar{p} explains $10\% \pm 8\%$ of the $\bar{\zeta}$ variance. Surface loading (the combination of \bar{q} and \bar{p} forcing)
 350 explains $14\% \pm 11\%$ of the variance in the data. Collectively, all three local forcing factors taken
 351 together account for $27\% \pm 14\%$ of the $\bar{\zeta}$ variance.⁷

⁷The variance contributions of the individual predictors are not entirely additive, since they are not wholly independent and there is some correlation between them. However, the relative roles of the respective forcings can nevertheless be meaningfully estimated (albeit with uncertainty) because the least-squares problem is generally well posed. After normalizing the predictors to unit variance, the condition number of their covariance matrix is 3.3. This is on the same order as the range of 1.4–2.5 (99% confidence interval) we determine through repeated simulations of four independent random, standard-normal time series (and their Hilbert transforms) with the same length as the observations (not shown).

352 Regression coefficients computed empirically from the data are consistent with values expected
 353 theoretically from first principles (Table 4). For example, the linear regression yields a scaling
 354 factor of $1.5 \pm 0.5 \text{ m Pa}^{-1}$ and a phase angle of 30 ± 25 degrees between τ and $\bar{\zeta}$. This is consistent
 355 with the theoretical ranges of $1.0\text{--}1.3 \text{ m Pa}^{-1}$ and $5\text{--}38$ degrees anticipated from Eqs. (7) and (8).
 356 The regression analysis also suggests a substantial departure from the inverted-barometer response,
 357 manifested in a scaling of $0.8 \pm 0.5 \text{ cm mb}^{-1}$ and a phase of 65 ± 52 degrees between \bar{p} and $\bar{\zeta}$. This
 358 overlaps with the ranges of $0.1\text{--}0.5 \text{ cm mb}^{-1}$ and $56\text{--}87$ degrees expected from Eqs. (11) and (12).
 359 (Recall that the altimeter data have been adjusted for an inverted barometer and that our theory was
 360 developed for ζ , which has the inverted-barometer effect already removed.) This provides evidence
 361 that the results of the multiple linear regression indicate true causal relationships between forcing
 362 and response.

363 Regression results and analytical theory suggest that these relationships can be out of phase, such
 364 that the forcings lead the response by a significant amount (Table 4). To quantify the importance of
 365 out-of-phase behavior, we perform another multiple linear regression analysis, this time omitting
 366 Hilbert transforms and forcing by p from the input [cf. Eq. (13)]. Physically, this alternative
 367 regression model assumes an equilibrium response, and corresponds to the steady state ($\omega \rightarrow 0$)
 368 limit of the governing equations, viz. [cf. Eq. (3)],

$$\bar{\zeta} = \zeta_0 + \frac{L}{\rho g h} \tau + \frac{\lambda}{\sigma^2} \bar{q}. \quad (16)$$

369 This alternate model accounts for slightly less of the $\bar{\zeta}$ data variance ($62\% \pm 10\%$; 95% confidence
 370 interval). This result demonstrates that a majority of the $\bar{\zeta}$ data variance explained by the original
 371 multiple linear regression model [Eq. (13)] is attributable to equilibrium processes and in-phase (or
 372 antiphase) relationships between the forcing and the response, but also that allowing for transient
 373 processes [the time derivatives in Eqs. (1) and (2)] and more general phase relationships between

374 forcing and response leads to a modest, but significant, improvement in terms of explaining $\bar{\zeta}$ data
375 variance.

376 *c. Relation to Indian Ocean circulation and climate, and potential predictability*

377 Nonlocal forcing by ζ_0 is the most important contributor to $\bar{\zeta}$ variability (Figure 6b). What is the
378 nature of these fluctuations at the boundary in the Gulf of Oman? How do they relate to larger-scale
379 circulation and climate? To clarify their origin, we compute correlation coefficients between ζ_0
380 and either ζ or its Hilbert transform $\mathcal{H}(\zeta)$ at every altimetric grid point over the Indian Ocean.
381 Correlations between ζ_0 and ζ identify regions where ζ is in phase or anti-phase (i.e., 180 degrees
382 out of phase) with ζ_0 , whereas correlations between ζ_0 and $\mathcal{H}(\zeta)$ indicate regions where ζ is in
383 quadrature (90 degrees out of phase) or anti-quadrature (270 degrees out of phase) with ζ_0 .

384 In general, ζ_0 is uncorrelated with ζ and $\mathcal{H}(\zeta)$ away from the coast and the equator (Figure 7),
385 suggesting that ζ_0 is unrelated to the dominant ζ variability in these open-ocean regions. However,
386 we observe patterns of significant correlation and anti-correlation along the coast and equator. For
387 example, ζ_0 is correlated with ζ along Pakistan, western India, and Sri Lanka; correlated with
388 $\mathcal{H}(\zeta)$ along eastern India, Bangladesh, and Myanmar; correlated with $\mathcal{H}(\zeta)$ and anti-correlated
389 with ζ along Thailand, Malaysia, and Sumatra; and anti-correlated with $\mathcal{H}(\zeta)$ along the western
390 equatorial Indian Ocean between Somalia and the Maldives (Figure 7).

391 These patterns suggest wave propagation along equatorial and coastal waveguides. For example,
392 the correlation between ζ_0 and $\mathcal{H}(\zeta)$ along Bangladesh suggests that ζ_0 lags ζ in this region by 90
393 degrees (one quarter of a period), whereas anti-correlation between ζ_0 and $\mathcal{H}(\zeta)$ in the western
394 equatorial Indian Ocean hints that regional ζ leads ζ_0 by 270 degrees (three quarters of a period).
395 Supposing propagation is eastward along the equator and counterclockwise along the coast (in the
396 Northern Hemisphere), and assuming intraseasonal periods of 60–180 days, we estimate that these

397 phase leads and lags imply propagation speeds of $\sim 1\text{--}3 \text{ m s}^{-1}$. These values are consistent with
398 basic expectations for equatorial waves and coastally trapped waves (e.g., Gill, 1982; Hughes et al.,
399 2019). Indeed, past studies argue that low-latitude wind forcing associated with the Madden-Julian
400 oscillation (MJO) and phases of the monsoon excite wave responses that effect intraseasonal sea-
401 level variability along Sumatra and Java (Iskandar et al., 2005), the Bay of Bengal (Cheng et al.,
402 2013), and India and Sri Lanka (Suresh et al., 2013; Dhage and Strub, 2016). Our results reinforce
403 these past findings, and suggest that these nonlocal forcing effects mediated by large-scale wave
404 responses continue on and are communicated to the Persian Gulf.

405 We perform a similar analysis with GRACE data. Correlations between ζ_0 and either GRACE
406 R_m or its Hilbert transform $\mathcal{H}(R_m)$ over the Indian Ocean are shown in Figure 8. While there
407 is essentially no meaningful correlation anywhere between ζ_0 and $\mathcal{H}(R_m)$, there is significant
408 correlation between ζ_0 and GRACE R_m broadly over much of the Indian Ocean (Figure 8). This
409 suggests that ζ_0 is also related to a basin-scale equilibrium response in addition to the more transient
410 wave adjustments trapped to the coast and the equator suggested by the altimetry data (Figure 7).
411 Indeed, the correlation pattern between ζ_0 and R_m (Figure 8a) is similar to the spatial structure
412 of the intraseasonal fluctuation of the Indian Ocean identified by Rohith et al. (2019) based on
413 data from bottom-pressure recorders, GRACE, and a general circulation model. They argue that
414 wind-curl fluctuations at 30–80-day periods over the Wharton basin associated with the MJO excite
415 planetary and topographic Rossby wave responses that lead to a basin-wide barotropic variation
416 that is confined to the Indian Ocean by bathymetric contours. Our results provide observational
417 evidence that this large-scale intraseasonal fluctuation affects variability not only over the deep
418 Indian Ocean but also within its shallow marginal seas.

419 Wave propagation apparent in Figure 7 hints that ζ_0 variability may be predictable to some extent.
420 That is, armed with upstream ζ information, it may be possible to anticipate ζ_0 variance in advance.

421 To test this possibility, we compute lagged correlation coefficients between ζ_0 and ζ at earlier times
422 over the Indian Ocean. Results are shown in Figure 9 for lead times of 1 and 2 months. Considering
423 a 1-month lead time, we find positive correlations between ζ_0 and ζ upstream along the Indian
424 Subcontinent and Maritime Continent, from eastern India to Sumatra, and negative correlations
425 over the western Equatorial Indian Ocean between Somalia and the Maldives (figure 9a). Indeed,
426 the pattern of correlation between ζ_0 and ζ 1 month earlier is similar to the structure of correlation
427 between ζ_0 and $\mathcal{H}(\zeta)$ (cf. Figures 7b, 9a), suggesting a dominant timescale of ~ 4 months. Values
428 of 0.4–0.5 are apparent off Myanmar and Sumatra (Figure 9a), hinting that 16–25% of the variance
429 in ζ_0 can be predicted from ζ knowledge in these regions 1 month earlier. Considering a lead time
430 of 2 months, we observe that ζ_0 and ζ are largely uncorrelated, except for along Pakistan, western
431 India, and Sri Lanka, where negative coefficients between -0.3 and -0.4 are seen. This implies that
432 9–16% of the ζ_0 variance can be predicted from ζ observations along this coastline 2 months earlier.
433 Considering lead times of 3 months and longer, we detect no significant correlations between ζ_0
434 and ζ elsewhere (not shown), indicating that there is little skill in predictions of intraseasonal ζ_0
435 variability more than 2 months into the future from wave characteristics and ocean memory alone.

436 **5. Summary and discussion**

437 We studied intraseasonal variability in ocean dynamic sea level (ζ) over the Persian Gulf during
438 2002–2015 using satellite observations and other data (Figures 1, 2). Intraseasonal ζ variability
439 in the Persian Gulf manifests in a basin-wide, vertically coherent mode of fluctuation (Figures 3–
440 5). This large-scale mode is related to freshwater flux and barometric pressure over the Persian
441 Gulf, wind stress along the Strait of Hormuz, and nonlocal forcing embodied in ζ variations at
442 the boundary in the Gulf of Oman (Figure 6). The ζ boundary condition shows rich correlation
443 patterns with altimetry data upstream along the Indian Subcontinent, Maritime Continent, and

444 equatorial Indian Ocean (Figure 7), and with GRACE data broadly over the Indian Ocean (Figure 8),
445 suggesting an intimate connection between intraseasonal ζ variability in the Persian Gulf and
446 large-scale circulation and climate over the Indian Ocean mediated by equatorial-, Rossby-, and
447 coastal-wave processes identified previously (Cheng et al., 2013; Dhage and Strub, 2016; Iskandar
448 et al., 2005; Oliver and Thompson, 2010; Rohith et al., 2019; Suresh et al., 2013, 2016; Waliser et
449 al., 2003, 2004). Our results indicate that some intraseasonal ζ variance in the Persian Gulf may
450 be predictable a month or so in advance from upstream observations and the physics of coastal
451 wave propagation and ocean memory (Figure 9).

452 Our results establish the dominant magnitudes, scales, and mechanisms of intraseasonal sea-level
453 variability in the Persian Gulf, and thus build on findings from past works that emphasize seasonal
454 cycles and decadal trends (Al-Subhi, 2010; Alothman et al., 2014; Ayhan, 2020; El-Gindy, 1991;
455 El-Gindy and Eid, 1997; Hassanzadeh et al., 2007; Hosseinibalam et al., 2007; Sharaf El Din,
456 1990; Siddig et al., 2019; Sultan et al., 1995a, 2000). Our study demonstrates that GRACE
457 satellite retrievals are informative for interrogating coastal sea level over a semi-enclosed marginal
458 sea, thereby complementing previous efforts that demonstrate the value of GRACE data in other
459 marginal seas (Feng et al., 2012, 2014; Fenoglio-Marc et al., 2006, 2012; Landerer and Volkov,
460 2013; Loomis and Luthcke, 2017; Piecuch and Ponte, 2015; Piecuch et al., 2018; Tregoning et
461 al., 2008; Wahr et al., 2014; Wang et al., 2015; Wouters and Chambers, 2010), and encouraging
462 further exploration of GRACE data in the Persian Gulf at other timescales.

463 This investigation advances knowledge of sea-level variability in the Persian Gulf. It also paves
464 the way for future studies, pointing to open questions. For example, we developed and tested a
465 theory for a horizontally uniform fluctuation of the Persian Gulf. However, the leading mode of
466 intraseasonal ζ variability in the region exhibits spatial structure, such that magnitudes are larger in
467 the northwest and smaller in the southeast of the Persian Gulf (Figures 3, 5). We hypothesized that

468 this spatial structure could arise from local forcing by river runoff or wind stress over the Persian
469 Gulf. Future studies based on high-resolution ocean models should test this hypothesis and identify
470 the controls on spatial structure. It also remains to quantify whether baroclinic effects and steric
471 processes contribute to the dominant intraseasonal ζ variability in the Persian Gulf. Future studies
472 could explore this topic by comparing differences between altimetry and GRACE data, which are
473 potentially informative of steric processes, to sea-level changes expected from a passive response
474 to local surface heat flux (e.g., Cabanes et al., 2006).

475 We determined that dynamic response to barometric pressure and freshwater flux is a secondary
476 but nevertheless significant contributor to intraseasonal ζ variability in the Persian Gulf (Figure 6).
477 This is interesting, given that the barotropic ocean response to surface loading is generally expected
478 to be isostatic on timescales longer than a few days (e.g., Wunsch and Stammer, 1997; Ponte, 2006).
479 In our model physics, the dynamic response is permitted by friction through the Strait of Hormuz.
480 Our finding that freshwater flux elicits a ζ response on the order of a few mm (Figure 6) is consistent
481 with the basic ζ magnitudes simulated for this region across subdaily to annual timescales by Ponte
482 (2006) using a 1-year simulation from a global barotropic ocean general circulation model forced
483 with evaporation and precipitation (Hirose et al., 2001); however, that model was designed for
484 global studies, and it used coarse resolution ($\sim 1^\circ$) and a large friction coefficient ($2 \times 10^{-2} \text{ m s}^{-1}$),
485 which may not accurately capture important physics in and around the Persian Gulf. Future studies
486 using high-resolution ocean models would be informative for clarifying the nature of intraseasonal
487 ζ variation in the Persian Gulf and the role of surface loading. Also relevant here is the fact that the
488 non-isostatic response to barometric pressure is roughly in quadrature with the forcing (Table 4).
489 This highlights the importance of considering phase information when testing for departures from
490 a pure inverted-barometer response in sea-level data (e.g., Mathers and Woodworth, 2001, 2004).

491 Past studies argue that low-latitude wind forcing of the Indian Ocean related to large-scale
492 climate modes excites wave responses that effect intraseasonal sea-level variability along the
493 Indian Subcontinent and Maritime Continent, from Sumatra to western India (Cheng et al., 2013;
494 Dhage and Strub, 2016; Iskandar et al., 2005; Suresh et al., 2013). We provide evidence that
495 these coastal-trapped waves continue propagating downstream and influence sea level in the Gulf
496 of Oman and Persian Gulf (Figure 7). We acknowledge that, while it suggests wave propagation,
497 Figure 7 could alternatively indicate the spatial scales of the atmospheric forcing. For example,
498 large-scale wind forcing along the equator and off the southern tip of the Indian subcontinent could
499 simultaneously excite equatorial waves and coastal waves propagating in the cyclonic sense along
500 the west coast of the Indian subcontinent (e.g., Suresh et al., 2013; Dhage and Strub, 2016). Future
501 studies should identify the dominant centers of action of atmospheric forcing of intraseasonal ζ
502 variability in the Persian Gulf, and whether coastal-trapped waves arriving in the Gulf of Oman
503 have their origin in equatorial waves that impinged on the Maritime Continent. Our results also
504 raise questions of whether such wave signals are felt even farther downstream along the coastal
505 waveguide, for example, in the Red Sea. Previous investigations of sea-level variability in the
506 Red Sea on timescales from days to decades largely emphasize the role of more local forcing
507 (Abdelrahman, 1997; Churchill et al., 2018; Cromwell and Smeed, 1998; Osman, 1984; Patzert,
508 1974; Sofianos and Johns, 2001; Sultan and Elghribi 2003; Sultan et al., 1995b, 1995c, 1996).
509 However, recent work by Alawad et al. (2017, 2019) suggests that mean sea-level variability in the
510 Red Sea is partly related to large-scale modes of climate variability. These authors reason that this
511 relationship is mediated by westward propagation of off-equatorial Rossby waves originating in the
512 eastern tropical Indian Ocean. Based on our results, we hypothesize that coastal-wave propagation
513 may also play a role in facilitating this relationship between sea level in the Red Sea and large-scale
514 climate. We leave it to future studies to test this hypothesis.

515 *Acknowledgments.* The authors acknowledge support from NASA through the Sea Level Change
516 Team (grant 80NSSC20K1241) and GRACE Follow-On Science Team (grant 80NSSC20K0728).

517 *Data availability statement.* Data are available through links provided in Table 1. Matlab codes
518 used for processing the data and producing the results are available from the corresponding author
519 upon request.

520 **References**

521 Abdelrahman, S. M., 1997: Seasonal Fluctuations of Mean Sea Level at Gizan, Red Sea. *Journal*
522 *of Coastal Research*, 13(4), 1166–1172,

523 Ablain, M., A. Cazenave, G. Larnicol, M. Balmaseda, P. Cipollini, Y. Faugère, M. J. Fernandes,
524 O. Henry, J. A. Johannessen, P. Knudsen, O. Andersen, J. Legeais, B. Meyssignac, N. Picot,
525 M. Roca, S. Rudenko, M. G. Scharffenberg, D. Stammer, G. Timms, and J. Benveniste, 2015:
526 Improved sea level record over the satellite altimetry era (1993?2010) from the Climate Change
527 Initiative project. *Ocean Science*, 11, 67–82, <https://doi.org/10.5194/os-11-67-2015>.

528 Adler, R. F., G. J. Huffman, A. Chang, R. Ferraro, P. Xie, J. Janowiak, B. Rudolf, U.
529 Schneider, S. Curtis, D. Bolvin, A. Gruber, J. Susskind, and P. Arkin, 2003: The Ver-
530 sion 2 Global Precipitation Climatology Project (GPCP) Monthly Precipitation Analysis
531 (1979-Present). *Journal of Hydrometeorology*, 4,1147–1167, [https://doi.org/10.1175/1525-](https://doi.org/10.1175/1525-7541(2003)004<1147:TVGPCP>2.0.CO;2)
532 [7541\(2003\)004<1147:TVGPCP>2.0.CO;2](https://doi.org/10.1175/1525-7541(2003)004<1147:TVGPCP>2.0.CO;2)

533 al-Chalabi, I., 2007: Oil. The Geopolitics of Oil and Iraq. *New England Journal of Public Policy*,
534 *21(2)*, 136–139, <https://scholarworks.umb.edu/nejpp/vol21/iss2/13>.

- 535 Al-Jeneid, S., Bahnassy, M., Nasr, S., and El Raey, M., 2008: Vulnerability assessment and
536 adaptation to the impacts of sea level rise on the Kingdom of Bahrain. *Mitigation and Adaptation*
537 *Strategies for Global Change*, 13, 87–104, <https://doi.org/10.1007/s11027-007-9083-8>.
- 538 Al-Subhi, A. M., 2010: Tide and sea level characteristics at Juaymah, west coast of the
539 Arabian Gulf. *Journal of King Abdulaziz University Marine Science*, 21(1), 133–149,
540 <https://doi.org/10.4197/mar.21-1.8>.
- 541 Alawad, K. a. I., A. M. Al-Subhi, M. A. Alsaafani, and T. M. Alraddadi, 2017: Signatures of
542 Tropical climate modes on the Red Sea and Gulf of Aden Sea Level. *Indian Journal of Geo*
543 *Marine Sciences*, 46(10), 2088–2096, <http://nopr.niscair.res.in/handle/123456789/42751>.
- 544 Alawad, K. a. I., A. M. Al-Subhi, M. A. Alsaafani, M. Ionita, and G. Lohmann, 2019: Large-Scale
545 Mode Impacts on the Sea Level over the Red Sea and Gulf of Aden. *Remote Sensing*, 11, 2244,
546 <https://doi.org/10.3390/rs11192224>.
- 547 Alothman, A. O., M. S. Bos, R. M. S. Fernandes, and M. E. Ayhan, 2014: Sea level
548 rise in the north-western part of the Arabian Gulf. *Journal of Geodynamics*, 81, 105–110,
549 <https://doi.org/10.1016/j.jog.2014.09.002>.
- 550 Amin, A., and K. Bankher, 1997: Causes of land subsidence in the Kingdom of Saudi Arabia.
551 *Natural Hazards*, 16(1), 57–63, <https://doi.org/10.1023/A:1007942021332>.
- 552 Ayhan, M. E., 2020: Dynamic harmonic regression modeling for monthly mean sea levels at tide
553 gauges within the Arabian Gulf. *Journal of Geodesy*, 94(46), [https://doi.org/10.1007/s00190-](https://doi.org/10.1007/s00190-020-01371-x)
554 [020-01371-x](https://doi.org/10.1007/s00190-020-01371-x).
- 555 Barnes, J., and A. M. Jaffe, 2006: The Persian Gulf and the Geopolitics of Oil. *Survival: Global*
556 *Politics and Strategy*, 48(1), 143–162, <https://doi.org/10.1080/00396330600594348>.

- 557 Barzandeh, A., N. Eshghi, F. Hosseinibalam, and S. Hassanzadeh, 2018: Wind-driven coastal
558 upwelling along the northern shoreline of the Persian Gulf. *Bollettino di Geofisica Teorica ed*
559 *Applicata*, 59(3), 301–302, <https://doi.org/10.4430/bgta0235>.
- 560 Bingham, R. J., and C. W. Hughes, 2008: The relationship between sea-level and bottom pressure
561 variability in an eddy permitting ocean model. *Geophysical Research Letters*, 35, L03602,
562 <https://doi.org/10.1029/2007GL032662>.
- 563 Burgos, A. G., B. D. Hamlington, P. R. Thompson, and R. D. Ray: Future Nuisance Flooding
564 in Norfolk, VA, From Astronomical Tides and Annual to Decadal Internal Climate Variability.
565 *Geophysical Research Letters*, 45, 12432–12439, <https://doi.org/10.1029/2018GL079572>.
- 566 Cabanes, C., T. Huck, and A. Colin de Verdière, 2006: Contributions of Wind Forcing and
567 Surface Heating to Interannual Sea Level Variations in the Atlantic Ocean. *Journal of Physical*
568 *Oceanography*, 36, 1739–1750.
- 569 Carrère, L., and F. Lyard, 2003: Modeling the barotropic response of the global ocean to at-
570 mospheric wind and pressure forcing—comparisons with observations. *Geophysical Research*
571 *Letters*, 30(6), 1275, <https://doi.org/10.1029/2002GL016473>.
- 572 Carrère, L., Y. Faugère, and M. Ablain, 2016: Major improvement of altimetry sea level estima-
573 tions using pressure-derived corrections based on ERA-Interim atmospheric reanalysis. *Ocean*
574 *Science*, 12, 825–842, <https://doi.org/10.5194/os-12-825-2016>.
- 575 Chao, S.-Y., T. W. Kao, and K. R. Al-Hajri, 1992: A numerical investigation of the cir-
576 culation in the Arabian Gulf. *Journal of Geophysical Research*, 97(C7), 11219–11236.
577 <https://doi.org/10.1029/92JC00841>.

578 Cheng, X., S.-P. Xie, J. P. McCreary, Y. Qi, Y., and Y. Du, 2013: Intraseasonal variability of sea
579 surface height in the Bay of Bengal. *Journal of Geophysical Research Oceans*, *118*(2), 816–430,
580 <https://doi.org/10.1002/jgrc.20075>.

581 Churchill, J. H., Abualnaja, Y., Limeburner, R., and Nellayaputhenpeedika, M., 2018: The dynam-
582 ics of weather-band sea level variations in the Red Sea. *Regional Studies in Marine Science*, *24*,
583 336–342, <https://doi.org/10.1016/j.rsma.2018.09.006>.

584 Cromwell, D., and Smeed, D. A., 1998: Altimetric observations of sea level cycles near
585 the Strait of Bab al Mandab. *International Journal of Remote Sensing*, *19*(8), 1561–1578,
586 <https://doi.org/10.1080/014311698215351>.

587 Dangendorf, S., A. Arns, J. G. Pinto, P. Ludwig, and J. Jensen, 2016: The exceptional influence of
588 storm ‘Xaver’ on design water levels in the German Bight. *Environmental Research Letters*, *11*,
589 054001, <https://doi.org/10.1088/1748-9326/11/5/054001>.

590 Dangendorf, S., C. Hay, F. M. Calafat, M. Marcos, C. G. Piecuch, K. Berk, and J. Jensen, 2019:
591 Persistent acceleration in global sea-level rise since the 1960s. *Nature Climate Change*, *9*,
592 705–710, <https://doi.org/10.1038/s41558-019-0531-8>.

593 Dee, D. P., S. M. Uppala, A. J. Simmons, P. Berrisford, P. Poli, S. Kobayashi, U. Andrae, M. A.
594 Balmaseda, G. Balsamo, P. Bauer, P. Bechtold, A. C. M. Beljaars, L. van de Berg, J. Bidlot,
595 N. Bormann, C. Delsol, R. Dragani, M. Fuentes, A. J. Geer, L. Haimberger, S. B. Healy, H.
596 Hersbach, E. V. Hólm, L. Isaksen, P. Kållberg, M. Köhler, M. Matricardi, A. P. McNally, B. M.
597 Monge-Sanz, J.-J. Morcrette, B.-K. Park, C. Peubey, P. de Rosnay, C. Tavalato, J.-N. Thépaut,
598 and F. Vitart, 2011: The ERA-Interim reanalysis: configuration and performance of the data
599 assimilation system. *Quarterly Journal of the Royal Meteorological Society*, **137**, 553–597,
600 <https://doi.org/10.1002/qj.828>.

601 Dhage, L., and P. T. Strub, 2016: Intra-seasonal sea level variability along the
602 west coast of India. *Journal of Geophysical Research Oceans*, 121, 8172–8188,
603 <https://doi.org/10.1002/2016JC011904>.

604 Efron, B., and T. Hastie, 2016: *Computer Age Statistical Inference: Algorithms, Evidence, and*
605 *Data Science*, Cambridge University Press, 495 pp.

606 El-Gindy, A. A. H., 1991: Sea level variations and their relations to the meteorological factors in
607 the Arab Gulf area with stress on monthly means. *International Hydrographic Review*, 68(1),
608 109–125.

609 El-Gindy, A. A., and F. M. Eid, 1997: The seasonal variations of sea level due to density variations
610 in the Arabian Gulf and Gulf of Oman. *Pakistan Journal of Marine Sciences*, 6(1–2), 1–12.

611 Emery, K. O., 1956: Sediments and water in the Persian Gulf. *Bulletin of the American Association*
612 *of Petroleum Geologists*, 40(10), 2354–2383, [https://doi.org/10.1306/5CEAE595-16BB-11D7-](https://doi.org/10.1306/5CEAE595-16BB-11D7-8645000102C1865D)
613 [8645000102C1865D](https://doi.org/10.1306/5CEAE595-16BB-11D7-8645000102C1865D).

614 Feng, W., M. Zhong, and H. Z. Xu, 2012: Sea level variations in the South China Sea inferred
615 from satellite gravimetry, altimetry, and oceanographic data. *Science in China Series D*, 55, 10,
616 1696–1701, <https://doi.org/10.1007/s11430-012-4394-3>.

617 Feng, W., J.-M. Lemoine, M. Zhong, M., and H. T. Hsu, 2014: Mass-induced sea
618 level variations in the Red Sea from GRACE, steric-corrected altimetry, in situ bot-
619 tom pressure records, and hydrographic observations. *Journal of Geodynamics*, 78, 1–7.
620 <http://dx.doi.org/10.1016/j.jog.2014.04.008>.

621 Fenoglio-Marc, L., J. Kusche, and M. Becker, 2006: Mass variation in the Mediterranean Sea
622 from GRACE and its validation by altimetry, steric and hydrologic fields. *Geophysical Research*
623 *Letters*, 33(L19606), <https://doi.org/10.1029/2006GL026851>.

624 Fenoglio-Marc, L., R. Rietbroek, S. Grayek, M. Becker, J. Kusche, and E. Stanev, 2012: Wa-
625 ter mass variation in the Mediterranean and Black Seas. *Journal of Geodynamics*, 59–60,
626 <https://doi.org/10.1016/j.jog.2012.04.001>.

627 Frederikse, T., F. Landerer, L. Caron, S. Adhikari, D. Parkes, V. W. Humphrey, S. Dangendorf, P.
628 Hogarth, L. Zanna, L. Cheng, and Y.-H. Wu: The causes of sea-level rise since 1900. *Nature*,
629 584, 393–397, <https://doi.org/10.1038/s41586-020-2591-3>.

630 Gill, A. E., 1982: *Atmosphere-Ocean Dynamics*, Academic Press, 680 pp.

631 Gill, A. E., and P. P. Niiler, 1973: The theory of the seasonal variability in the ocean. *Deep-Sea*
632 *Research*, 20, 141–177, [https://doi.org/10.1016/0011-7471\(73\)90049-1](https://doi.org/10.1016/0011-7471(73)90049-1).

633 Gregory, J. M., S. M. Griffies, C. W. Hughes, J. A. Lowe, J. A. Church, I. Fukumori, N. Gomez,
634 R. E. Kopp, F. Landerer, G. Le Cozannet, R. M. Ponte, D. Stammer, M. E. Tamisiea, and R. S.
635 W. van de Wal, 2019: Concepts and Terminology for Sea Level: Mean, Variability and Change,
636 Both Local and Global. *Surveys in Geophysics*, 40, 1251–1289, [https://doi.org/10.1007/s10712-](https://doi.org/10.1007/s10712-019-09525-z)
637 [019-09525-z](https://doi.org/10.1007/s10712-019-09525-z).

638 Hassanzadeh, S., A. Kiasatpour, and F. Hosseinibalam, 2007: Sea-level response to atmospheric
639 forcing along the north coast of Persian Gulf. *Meteorology and Atmospheric Physics*, 95, 223–
640 237, <https://doi.org/10.1007/s00703-006-0213-8>.

641 Hirose, N., I. Fukumori, V. Zlotnicki, and R. M. Ponte, 2001: Modeling the high-
642 frequency barotropic response of the ocean to atmospheric disturbances: Sensitivity to forc-

643 ing, topography, and friction. *Journal of Geophysical Research*, 106(C12), 30987–30995,
644 <https://doi.org/10.1029/2000JC000763>.

645 Holgate, S. J., A. Matthews, P. L. Woodworth, L. J. Rickards, M. E. Tamisiea, E. Bradshaw, P.
646 R. Foden, K. M. Gordon, S. Jevrejeva, and J. Pugh, 2013: New Data Systems and Products
647 and the Permanent Service for Mean Sea Level. *Journal of Coastal Research*, 29(3), 493–504,
648 <https://doi.org/10.2112/JCOASTRES-D-12-00175.1>.

649 Hosseinibalam, F., S. Hassanzadeh, and A. Kiasatpour, 2007: Interannual variability and seasonal
650 contribution of thermal expansion to sea level in the Persian Gulf. *Deep-Sea Research Part I*,
651 54, 1474–1485, <https://doi.org/10.1016/j.dsr.2007.05.005>.

652 Hughes, C. W., I. Fukumori, S. M. Griffies, J. M. Huthnance, S. Minobe, P. Spence, K. R.
653 Thompson, and A. Wise, 2019: Sea Level and the Role of Coastal Trapped Waves in Medi-
654 ating the Influence of the Open Ocean on the Coast. *Surveys in Geophysics*, 40, 1467–1492,
655 <https://doi.org/10.1007/s10712-019-09535-x>.

656 Iskandar, I., W. Mardiansyah, Y. Masumoto, and T. Yamagata, 2005: Intraseasonal Kelvin waves
657 along the southern coast of Sumatra and Java. *Journal of Geophysical Research*, 110(C04013),
658 <https://doi.org/10.1029/2004JC002508>.

659 Johns, W. E., G. A. Jacobs, J. C. Kindle, S. P. Murray, and M. Carron, 1999: Arabian Marginal
660 Seas and Gulfs: report of a workshop held at Stennis Space Center, Miss., 11–13 May 1999.
661 University of Miami RSMAS Technical Report 2000-01, 60 pp.

662 Johns, W. E., F. Yao, D. B. Olson, S. A. Josey, J. P. Grist, and D. A. Smeed, 2003: Ob-
663 servations of seasonal exchange through the Straits of Hormuz and the inferred heat and

664 freshwater budgets of the Persian Gulf. *Journal of Geophysical Research*, 108(C12), 3991,
665 <https://doi.org/10.1029/2003JC001881>.

666 Kämpf, J., and M. Sadrinassab, 2006: The circulation of the Persian Gulf: a numerical study. *Ocean*
667 *Science*, 2, 27–41, <https://doi.org/10.5194/os-2-27-2006>.

668 Kopp, R. E., R. M. Horton, C. M. Little, J. X. Mitrovica, M. Oppenheimer, D. J. Ras-
669 mussen, B. H. Strauss, and C. Tebaldi, 2014: Probabilistic 21st and 22nd century sea-
670 level projections at a global network of tide-gauge sites. *Earth's Future*, 2, 383–406,
671 <https://doi.org/10.1002/2014EF000239>.

672 Kopp, R. E., R. M. DeConto, D. A. Bader, C. C. Hay, R. M. Horton, S. Kulp, M. Oppen-
673 heimer, D. Pollard, and B. H. Strauss, 2017: Evolving Understanding of Antarctic Ice-Sheet
674 Physics and Ambiguity in Probabilistic Sea-Level Projections. *Earth's Future*, 5, 1217–1233,
675 <https://doi.org/10.1002/2017EF000663>.

676 Landerer, F. W., and D. L. Volkov, 2013: The anatomy of recent large sea level
677 fluctuations in the Mediterranean Sea. *Geophysical Research Letters*, 40, 553–557,
678 <https://doi.org/10.1002/grl.50140>.

679 Landerer, F. W., F. M. Flechtner, H. Save, F. H. Webb, T. Bandikova, W. I. Bertiger, S. V.
680 Bettadpur, S. H. Byun, C. Dahle, H. Dobslaw, E. Fahnestock, N. Harvey, Z. Kang, G. L. H.
681 Kruizinga, B. D. Loomis, C. McCullough, M. Murböck, P. Nagel, M. Paik, N. Pie, S. Poole,
682 D. Strelakov, M. E. Tamisiea, F. Wang, M. M. Watkins, H.-Y. Wen, D. N. Wiese, and D.-N.
683 Yuan, 2020: Extending the Global Mass Change Data Record: GRACE Follow-On Instru-
684 ment and Science Data Performance. *Geophysical Research Letters*, 47(12), e2020GL088306,
685 <https://doi.org/10.1029/2020GL088306>.

686 Lafta, A. A., S. A. Altaei, and N. H. Al-Hashimi, 2020: Impacts of potential sea-level rise on tidal
687 dynamics in Khor Abdullah and Khor Al-Zubair, northwest of Arabian Gulf. *Earth Systems and*
688 *Environment*, 4, 93–105, <https://doi.org/10.1007/s41748-020-00147-9>.

689 Larson, A., 2007: Oil. The Geopolitics of Oil and Natural Gas. *New England Journal of Public*
690 *Policy*, 21(2), 215–219, <https://scholarworks.umb.edu/nejpp/vol21/iss2/18>.

691 Legeais, J.-F., M. Ablain, L. Zawadzki, H. Zuo, J. A. Johannessen, M. G. Scharffenberg, L.
692 Fenoglio-Marc, M. J. Fernandes, O. B. Andersen, S. Rudenko, P. Cipollini, G. D. Quartly, M.
693 Passaro, A. Cazenave, and J. Benveniste, 2017.: An improved and homogeneous altimeter sea
694 level record from the ESA Climate Change Initiative. *Earth System Science Data*, 10, 281–301,
695 <https://doi.org/10.5194/essd-10-281-2018>.

696 Long, X., M. J. Widlansky, F. Schloesser, P. R. Thompson, H. Annamalai, M. A. Merrifield, and
697 H. Yoon, 2020: Higher Sea Levels at Hawaii Caused by Strong El Niño and Weak Trade Winds.
698 *Journal of Climate*, 33, 3037–3059, <https://doi.org/10.1175/JCLI-D-19-0221.1>.

699 Loomis, B. D., and S. B. Luthcke, 2017: Mass evolution of Mediterranean, Black, Red, and Caspian
700 Seas from GRACE and altimetry: accuracy assessment and solution calibration. *Journal of*
701 *Geodesy*, 91, 195–206, <https://doi.org/10.1007/s00190-016-0952-3>.

702 Mathers, E. L., and P. L. Woodworth, 2001: Departures from the local inverse barometer model
703 observed in altimeter and tide gauge data and in a global barotropic numerical model. *Journal*
704 *of Geophysical Research*, 106(C4), 9657–6972, <https://doi.org/10.1029/2000JC000241>.

705 Mathers, E. L., and P. L. Woodworth, 2004: A study of departures from the inverse-barometer
706 response of sea level to air-pressure forcing at a period of 5 days. *Quarterly Journal of the Royal*
707 *Meteorological Society*, 130, 725–738, <https://doi.org/10.1256/qj.03.46>.

708 Nerem, R. S., B. D. Beckley, J. T. Fasullo, B. D. Hamlington, D. Masters, and G. T. Mitchum, 2018:
709 Climate-change-driven accelerated sea-level rise detected in the altimeter era. *Proceedings of the*
710 *National Academy of Sciences*, 115(9), 2022–2025, <https://doi.org/10.1073/pnas.1717312115> .

711 Oliver, E. C. J., and K. R. Thompson, 2010: Madden-Julian Oscillation and sea
712 level: local and remote forcing. *Journal of Geophysical Research*, 115(C01003),
713 <https://doi.org/10.1029/2009JC005337>.

714 Osman, M. M., 1984: Variation of sea level at Port-Sudan. *International Hydrographic Review*,
715 61(2).

716 Patzert, W. C., 1974: Wind-induced reversal in Red Sea circulation. *Deep-Sea Research*, 21(2),
717 109–121, [https://doi.org/10.1016/0011-7471\(74\)90068-0](https://doi.org/10.1016/0011-7471(74)90068-0).

718 Piecuch, C. G., and R. M. Ponte, 2015: A wind-driven nonseasonal barotropic fluctuation of the
719 Canadian inland seas. *Ocean Science*, 11, 175–185, <https://doi.org/10.5194/os-11-175-2015>.

720 Piecuch, C. G., Landerer, F. W., and R. M. Ponte, 2018: Tide gauge records reveal improved process-
721 ing of Gravity Recovery and Climate Experiment time-variable mass solutions over the coastal
722 ocean. *Geophysical Journal International*, 214, 1401–1412, <https://doi.org/10.1093/gji/ggy207>.

723 Piecuch, C. G., F. M. Calafat, S. Dangendorf, and G. Jordà, 2019: The Ability of Barotropic
724 Models to Simulate Historical Mean Sea Level Changes from Coastal Tide Gauge Data. *Surveys*
725 *in Geophysics*, 40, 1399–1435, <https://doi.org/10.1007/s10712-019-09537-9>.

726 Ponte, R. M., 1992: The Sea Level Response of a Stratified Ocean to Barometric Pres-
727 sure Forcing. *Journal of Physical Oceanography*, 22, 109–113, [https://doi.org/10.1175/1520-0485\(1992\)022<0109:TSLROA>2.0.CO;2](https://doi.org/10.1175/1520-0485(1992)022<0109:TSLROA>2.0.CO;2).

729 Ponte, R. M., 1994: Understanding the relation between wind- and pressure-
730 driven sea level variability. *Journal of Geophysical Research*, 99(C4), 8033–8039,
731 <https://doi.org/10.1029/94JC00217>.

732 Ponte, R. M., 2006: Oceanic Response to Surface Loading Effects Neglected
733 in Volume-Conserving Models. *Journal of Physical Oceanography*, 36, 426–434,
734 <https://doi.org/10.1175/JPO2843.1>.

735 Permanent Service for Mean Sea Level (PSMSL), 2020: “Tide Gauge Data”, Retrieved 1 Jul 2019
736 from <http://www.psmsl.org/data/obtaining/>.

737 Quartly, G. D., J.-F. Legeais, M. Ablain, L. Zawadzki, M. J. Fernandes, S. Rudenko, L. Carrère,
738 P. N. García, P. Cipollini, O. B. Andersen, J.-C. Poisson, S. Mbajon Njiche, A. Cazenave, and
739 J. Benveniste, 2017: A new phase in the production of quality-controlled sea level data. *Earth*
740 *System Science Data*, 9, 557–572, <https://doi.org/10.5194/essd-9-557-2017>.

741 Ray, R. D., and G. Foster, 2016: Future nuisance flooding at Boston caused by astronomical tides
742 alone. *Earth’s Future*, 4, 578–587, <https://doi.org/10.1002/2016EF000423>.

743 Reynolds, R. M., 1993: Physical oceanography of the Gulf, Strait of Hormuz, and the Gulf
744 of Oman—results from the *Mt Mitchell* Expedition. *Marine Pollution Bulletin*, 27, 35–59,
745 [https://doi.org/10.1016/0025-326X\(93\)90007-7](https://doi.org/10.1016/0025-326X(93)90007-7).

746 Rohith, B., A. Paul, F. Durand, L. Testut, S. Prerna, M. Afroosa, S. S. V. S. Ramkrishna, and
747 S. S. C. Shenoi, 2019: Basin-wide sea level coherency in the tropical Indian Ocean driven by
748 Madden-Julian Oscillation. *Nature Communications*, 10, 1257, [https://doi.org/10.1038/s41467-](https://doi.org/10.1038/s41467-019-09243-5)
749 [019-09243-5](https://doi.org/10.1038/s41467-019-09243-5).

- 750 Sharaf El Din, S. H., 1990: Sea level variation along the western coast of the Arabian Gulf.
751 *International Hydrographic Review*, 67(1), 103–109.
- 752 Siddig, N. A., A. M. Al-Subhi, and M. A. Alsaafani, 2019: Tide and mean sea level trend in the west
753 coast of the Arabian Gulf from tide gauges and multi-missions satellite altimeter. *Oceanologia*,
754 61, 401–411, <https://doi.org/10.1016/j.oceano.2019.05.003>.
- 755 Sofianos, S. S., and Johns, W. E., 2001: Wind induced sea level variability in the Red Sea.
756 *Geophysical Research Letters*, 28(16), 3175–3178, <https://doi.org/10.1029/2000GL012442>.
- 757 Sultan, S. A. R., F. Ahmad, N. M. Elghribi, and A. M. Al-Subhi, 1995a: An analy-
758 sis of Arabian Gulf mean sea level. *Continental Shelf Research*, 15(11/12), 1471–1482,
759 [https://doi.org/10.1016/0278-4343\(94\)00081-W](https://doi.org/10.1016/0278-4343(94)00081-W).
- 760 Sultan, S. A. R., Ahmad, F., and Elghribi, N. M., 1995b: Sea level variability in the central Red
761 Sea. *Oceanologica Acta*, 18(6).
- 762 Sultan, S. A. R., Ahmad, F., and El-Hassan, A., 1995c: Seasonal variations of the sea
763 level in the central part of the Red Sea. *Estuarine, Coastal and Shelf Science*, 40, 1–8,
764 [https://doi.org/10.1016/0272-7714\(95\)90008-X](https://doi.org/10.1016/0272-7714(95)90008-X).
- 765 Sultan, S. A. R., Ahmad, F., and Nassar, D., 1996: Relative contribution of external sources of
766 mean sea-level variations at Port Sudan, Red Sea. *Estuarine, Coastal and Shelf Science*, 42,
767 19–30, <https://doi.org/10.1006/ecss.1996.0002>.
- 768 Sultan, S. A. R., M. O. Moamar, N. M. El-Ghribi, and R. Williams, 2000: Sea level changes along
769 the Saudi coast of the Arabian Gulf. *Indian Journal of Marine Sciences*, 29, 191–200.
- 770 Sultan, S. A. R., and Elghribi, N. M., 2003: Sea level changes in the central part of the Red Sea.
771 *Indian Journal of Marine Sciences*, 32(2), 114–122.

- 772 Suresh, I., J. Vialard, M. Lengaigne, W. Han, J. McCreary, F. Durand, and P. M.
773 Muraleedharan, 2013: Origins of wind-driven intraseasonal sea level variations in the
774 North Indian Ocean coastal waveguide. *Geophysical Research Letters*, *40*, 5740–5744,
775 <https://doi.org/10.1002/2013GL058312>.
- 776 Suresh, I., Vialard, J., Izumo, T., Lengaigne, M., Han, W., McCreary, J., and Muraleedha-
777 ran, P. M., 2016: Dominant role of winds near Sri Lanka in driving seasonal sea level
778 variations along the west coast of India. *Geophysical Research Letters*, *43*, 7028–7035,
779 <https://doi.org/10.1002/2016GL069976>
- 780 Sweet, W. V., M. Menendez, A. Genz, J. Obeysekera, J. Park, and J. J. Marra, 2017: In Tide’s Way:
781 Southeast Florida’s September 2015 Sunny-day Flood. *Bulletin of the American Meteorological*
782 *Society*, *97*(12), S25–S30, <https://doi.org/10.1175/BAMS-D-16-0117.1>.
- 783 Swift, S. A., and A. S. Bower, 2003: Formation and circulation of dense water in the Persian/Arabian
784 Gulf. *Journal of Geophysical Research*, *108*(C1), 3004, <https://doi.org/10.1029/2002JC001360>.
- 785 Thoppil, P. G., and P. J. Hogan, 2010: A Modeling Study of Circulation and
786 Eddies in the Persian Gulf. *Journal of Physical Oceanography*, *40*, 2122–2134,
787 <https://doi.org/10.1175/2010JPO4227.1>.
- 788 Tregoning, P., K. Lambeck, and G. Ramillien, 2008: GRACE estimates of sea surface height
789 anomalies in the Gulf of Carpentaria, Australia. *Earth and Planetary Science Letters*, *271*,
790 241–244, <https://doi.org/10.1016/j.epsl.2008.04.018>.
- 791 Tsujino, H., S. Urakawa, H. Nakano, R. J. Small, W. M. Kim, S. G. Yeager, G. Danabasoglu, T.
792 Suzuki, J. L. Bamber, M. Bentsen, C. W. Böning, A. Bozec, E. P. Chassignet, E. Curchitser, F. B.
793 Dias, P. J. Durack, S. M. Griffies, Y. Harada, M. Ilicak, S. A. Josey, C. Kobayashi, S. Kobayashi, Y.

794 Komuro, W. G. Large, J. Le Sommer, S. J. Marsland, S. Masina, M. Scheinert, H. Tomita, M. Val-
795 divieso, and D. Yamazaki, 2018: JRA-55 based surface dataset for driving ocean?sea-ice models
796 (JRA55-do). *Ocean Modelling*, 130, 79–139, <https://doi.org/10.1016/j.ocemod.2018.07.002>.

797 Vinogradova, N. T., R. M. Ponte, and D. Stammer, 2007: Relation between sea level and bottom
798 pressure and the vertical dependence of oceanic variability. *Geophysical Research Letters*, 34,
799 L03608, <https://doi.org/10.1029/2006GL028588>.

800 Volkov, D. L., W. E. Johns, and T. B. Belonenko, 2016: Dynamic response of the Black Sea
801 elevation to intraseasonal fluctuations of the Mediterranean sea level. *Geophysical Research*
802 *Letters*, 43, 283–290, <https://doi.org/10.1002/2015GL066876>.

803 von Storch, H., and F. W. Zwiers, 1999: *Statistical Analysis in Climate Research*, Cambridge
804 University Press, 496 pp.

805 Wahr, J. W., D. A. Smeed, E. Leuliette, and S. Swenson, 2014: Seasonal variability of the Red
806 Sea, from satellite gravimetry, radar altimetry, and in situ observations. *Journal of Geophysical*
807 *Research Oceans*, 119, 5091–5104, <https://doi.org/10.1002/2014JC010161>.

808 Waliser, D. E., R. Murtugudde, and L. E. Lucas, 2003: Indo-Pacific Ocean response to atmospheric
809 intraseasonal variability: 1. Austral summer and the Madden-Julian Oscillation. *Journal of*
810 *Geophysical Research*, 108(C5), 3160, <https://doi.org/10.1029/2002JC001620>.

811 Waliser, D. E., R. Murtugudde, and L. E. Lucas, 2003: Indo-Pacific Ocean response to atmo-
812 spheric intraseasonal variability: 2. Boreal summer and the Intraseasonal Oscillation. *Journal*
813 *of Geophysical Research*, 109(C03030), 3160, <https://doi.org/10.1029/2003JC002002>.

814 Wang, J., J. Wang, and X. Cheng, 2015: Mass-induced sea level variations in the Gulf of Carpen-
815 taria. *Journal of Oceanography*, 71, 449–461, <https://doi.org/10.1007/s10872-015-0304-6>.

- 816 Watkins, M. M., D. N. Wiese, D.-H. Yuan, C. Boening, and F. W. Landerer, 2015: Im-
817 proved methods for observing Earth's time variable mass distribution with GRACE using
818 spherical cap mascons. *Journal of Geophysical Research: Solid Earth*, 120, 2648–2671,
819 <https://doi.org/10.1002/2014JB011547>.
- 820 Wiese, D. N., F. W. Landerer, and M. M. Watkins, 2016: Quantifying and reducing leakage errors
821 in the JPL RL05M GRACE mascon solution. *Water Resources Research*, 52(9), 7490–7502,
822 <https://doi.org/10.1002/2016WR019344>.
- 823 Wouters, B., and D. Chambers, 2010: Analysis of seasonal ocean bottom pressure vari-
824 ability in the Gulf of Thailand from GRACE. *Global and Planetary Change*, 74, 76–81,
825 <https://doi.org/10.1016/j.gloplacha.2010.08.002>.
- 826 Wunsch, C., and D. Stammer, 1997: Atmospheric loading and the “inverted barometer” effect.
827 *Reviews in Geophysics*, 35(1), 79–107, <https://doi.org/10.1029/96RG03037>.
- 828 Yao, F., and W. E. Johns, 2010: A HYCOM modeling study of the Persian Gulf: 1.
829 Model configurations and surface circulation. *Journal of Geophysical Research*, 115(C11017),
830 <https://doi.org/10.1029/2009JC005781>.
- 831 Yu, L., and R. A. Weller, 2007: Objectively Analyzed Air-Sea Heat Fluxes for the Global Ice-
832 Free Oceans (1981–2005). *Bulletin of the American Meteorological Society*, 88(4), 527–540,
833 <https://doi.org/10.1175/BAMS-88-4-527>.

834 **LIST OF TABLES**

835 **Table 1.** Data sources. All websites are current as of this writing. 41

836 **Table 2.** Description of tide-gauge records. Asterisk indicates metric data without com-
 837 plete datum histories. 42

838 **Table 3.** Descriptions of and, where applicable, reasonable values for variables and
 839 parameters in governing equations. [†]Values of the friction coefficient r are
 840 uncertain. Previous studies variously use values ranging from as small as
 841 $4 \times 10^{-5} \text{ m s}^{-1}$ (e.g., Ponte, 1994) to as large as $2 \times 10^{-2} \text{ m s}^{-1}$ (e.g., Ponte,
 842 2006). Values in the table represent a reasonable, physically plausible range
 843 based on choices made in previous studies. 43

844 **Table 4.** Estimates of the scaling coefficients (z_j) and phase angles (θ_j) in Eq. (4). The
 845 theoretical ranges are determined by averaging Eqs. (5)–(12) over the range
 846 $\omega = 2\pi / (6 \text{ months})$ to $2\pi / (2 \text{ months})$ using the constant values for σ , L , ρ ,
 847 g , and H and the minimum and maximum values for λ tabulated in Table 3.
 848 Empirical values are determined through multiple linear regression involving $\bar{\zeta}$
 849 and $\bar{\zeta}_0$ from altimetry, τ and \bar{p} from ERA-Interim, and \bar{q} based on JRA55-do,
 850 GPCP, and OAFflux, and are presented as 95% confidence intervals estimated
 851 based on bootstrapping. Scaling coefficients are given to one decimal point and
 852 phase angles are rounded to the nearest degree. 44

Data set	Location
Altimetry	ftp://anon-ftp.ceda.ac.uk/neodc/esacci/sea_level/data/L4/MSLA/v2.0/
GRACE	https://podaac.jpl.nasa.gov/dataset/TELLUS_GRAC-GRFO_MASCON_CRI_GRID_RL06_V2
Tide gauges	https://www.psmsl.org/data/obtaining/complete.php
ERA-Interim	http://cmip5.whoi.edu/?page_id=566
GPCP	https://psl.noaa.gov/data/gridded/data.gpcp.html
OAFlux	ftp://ftp.whoi.edu/pub/science/oaflux/data_v3/monthly/evaporation/
JRA55-do	http://amaterasu.ees.hokudai.ac.jp/~tsujino/JRA55-do-suppl/runoff/

TABLE 1. Data sources. All websites are current as of this writing.

Station Name	Nation	PSMSL Identifier	Longitude (°E)	Latitude (°N)	Span	Completeness
Mina Sulman	Bahrain	1494	50.6	26.2	1979–2006	66.1%
Emam Hassan*	Iran	1868	50.3	29.8	1995–2006	91.7%
Bushehr*	Iran	1939	50.8	28.9	2004–2006	100.0%
Kangan*	Iran	1869	52.1	27.8	1995–2006	98.6%
Shahid Rajaei*	Iran	1870	56.1	27.1	1995–2006	100.0%

TABLE 2. Description of tide-gauge records. Asterisk indicates metric data without complete datum histories.

Parameter	Description	Value
ζ	Ocean Dynamic Sea Level	—
τ	Mean Wind Stress Along Strait of Hormuz	—
q	Surface Freshwater Flux	—
p	Barometric Pressure	—
ζ_0	Ocean Dynamic Sea Level in Gulf of Oman	—
$\bar{\cdot}$	Spatial Average over Persian Gulf	—
S	Surface Area of Persian Gulf	$2.2 \times 10^5 \text{ km}^2$
H	Average Depth of Persian Gulf	30 m
L	Length of Strait of Hormuz	500 km
W	Width of Strait of Hormuz	100 km
g	Gravitational Acceleration	9.81 m s^{-2}
ρ	Ocean Density	1029 kg m^{-3}
r	Friction Coefficient [†]	$1 \times 10^{-3} - 1 \times 10^{-2} \text{ m s}^{-1}$
σ	Inverse Resonance Timescale	$1.8 \times 10^{-5} \text{ s}^{-1}$
λ	Inverse Frictional Timescale	$3.3 \times 10^{-5} - 3.3 \times 10^{-4} \text{ s}^{-1}$

853 TABLE 3. Descriptions of and, where applicable, reasonable values for variables and parameters in governing
854 equations. [†]Values of the friction coefficient r are uncertain. Previous studies variously use values ranging from
855 as small as $4 \times 10^{-5} \text{ m s}^{-1}$ (e.g., Ponte, 1994) to as large as $2 \times 10^{-2} \text{ m s}^{-1}$ (e.g., Ponte, 2006). Values in the table
856 represent a reasonable, physically plausible range based on choices made in previous studies.

Parameter (Units)	Theoretical Range	Empirical Value
z_{ζ_0} (unitless)	0.8–1.0	1.0 ± 0.2
θ_{ζ_0} (degrees)	5–38	5 ± 10
z_{τ} (m Pa ⁻¹)	1.0–1.3	1.5 ± 0.5
θ_{τ} (degrees)	5–38	30 ± 25
$z_{\bar{q}}$ (days)	1.2–9.0	9.4 ± 3.7
$\theta_{\bar{q}}$ (degrees)	3–38	30 ± 27
$z_{\bar{p}}$ (cm mb ⁻¹)	0.1–0.5	0.8 ± 0.5
$\theta_{\bar{p}}$ (degrees)	56–87	65 ± 52

857 TABLE 4. Estimates of the scaling coefficients (z_j) and phase angles (θ_j) in Eq. (4). The theoretical ranges are
858 determined by averaging Eqs. (5)–(12) over the range $\omega = 2\pi / (6 \text{ months})$ to $2\pi / (2 \text{ months})$ using the constant
859 values for σ , L , ρ , g , and H and the minimum and maximum values for λ tabulated in Table 3. Empirical values
860 are determined through multiple linear regression involving $\bar{\zeta}$ and ζ_0 from altimetry, τ and \bar{p} from ERA-Interim,
861 and \bar{q} based on JRA55-do, GPCP, and OAFflux, and are presented as 95% confidence intervals estimated based
862 on bootstrapping. Scaling coefficients are given to one decimal point and phase angles are rounded to the nearest
863 degree.

864 **LIST OF FIGURES**

865 **Fig. 1.** Study area. White lines indicate national boundaries. Color shading identifies ocean depth.
 866 (Note the logarithmic scale bar and units of \log_{10} m.) Red dots denote locations of tide
 867 gauges (Table 2). Inset shows the study area in a global context. 46

868 **Fig. 2.** Monthly ocean dynamic sea level in the Persian Gulf between November 2002 and March
 869 2015 from satellite altimetry (gray, black, blue) and tide gauges (oranges). The satellite-
 870 altimetry data are spatially averaged over the Persian Gulf whereas the tide-gauge data
 871 represent a composite average over five sites (Figure 1). The raw monthly altimetry data are
 872 shown in gray, whereas the black and blue indicate the altimetry data with filtering applied to
 873 isolate nonseasonal and intraseasonal timescales, respectively. The tide-gauge data (orange)
 874 have been filtered to isolate intraseasonal periods and adjusted for the inverted-barometer
 875 effect. The standard deviations of the gray, black, blue, and orange time series are 4.7, 3.5,
 876 3.0, and 2.5 cm, respectively. 47

877 **Fig. 3.** (a.) Spatial pattern (eigenvector) of the first ζ EOF mode across the Persian Gulf from
 878 intraseasonal altimetry data. Units are cm. (b.) Local ζ variance explained by the first EOF
 879 mode. Units are percent of total variance. 48

880 **Fig. 4.** Principal-component time series of the first EOF modes from altimetry ζ (black) and GRACE
 881 R_m (blue) over the Persian Gulf. Time series have been normalized to unit variance (physical
 882 units are shown for the eigenvectors in Figures 3 and 5). 49

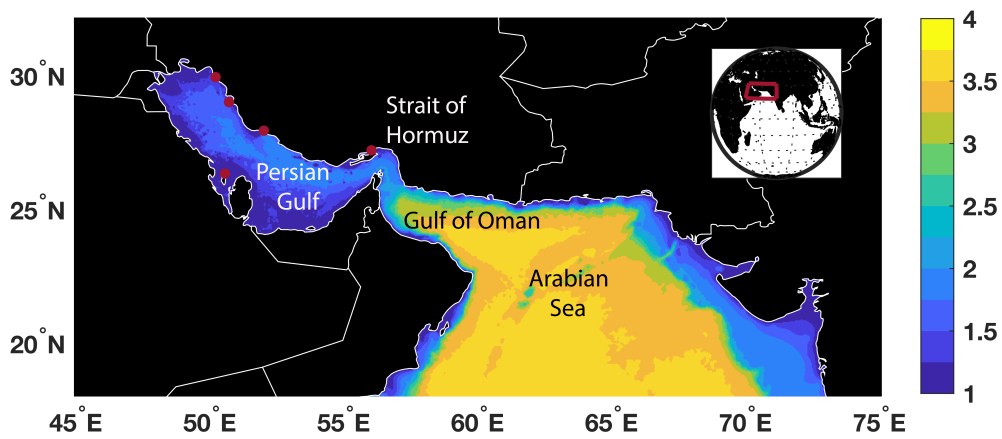
883 **Fig. 5.** (a.) Spatial pattern (eigenvector) of the first R_m EOF mode across the Persian Gulf from
 884 intraseasonal GRACE data. Units are cm. (b.) Local R_m variance explained by the first EOF
 885 mode. Units are percent of total variance. 50

886 **Fig. 6.** (a.) Time series of intraseasonal $\bar{\zeta}$ from satellite altimetry (black) and the results of the
 887 multiple linear regression model (blue). Units are cm. (b.) Breakdown of contributors to
 888 regression model—boundary forcing ζ_0 (orange), wind stress τ (green), freshwater flux \bar{q}
 889 (blue), and barometric pressure \bar{p} (red). Units are cm. 51

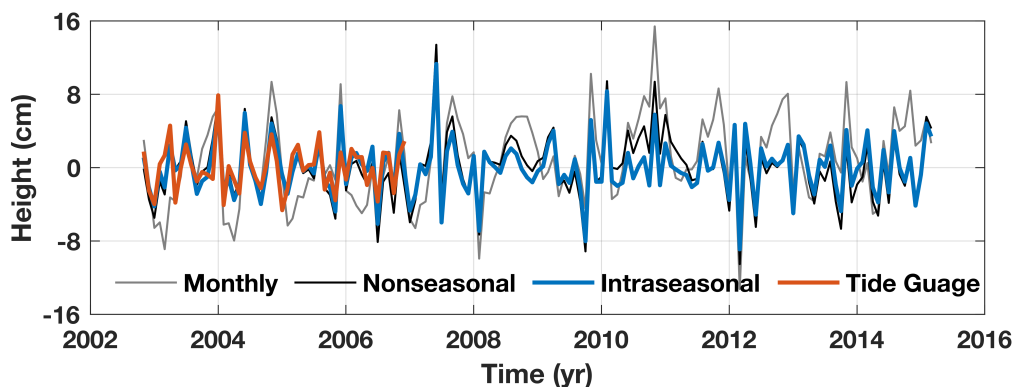
890 **Fig. 7.** Correlation coefficient between Gulf of Oman ζ_0 and either (a.) ζ from altimetry or (b.)
 891 $\mathcal{H}(\zeta)$ over the Indian Ocean. Light shading indicates values that are not distinguishable from
 892 zero at the 95% confidence level (assuming 100 degrees of freedom). 52

893 **Fig. 8.** Correlation coefficient between Gulf of Oman ζ_0 and either (a.) R_m from GRACE or (b.)
 894 $\mathcal{H}(R_m)$ over the Indian Ocean. Light shading indicates values that are not distinguishable
 895 from zero at the 95% confidence level (assuming 100 degrees of freedom). 53

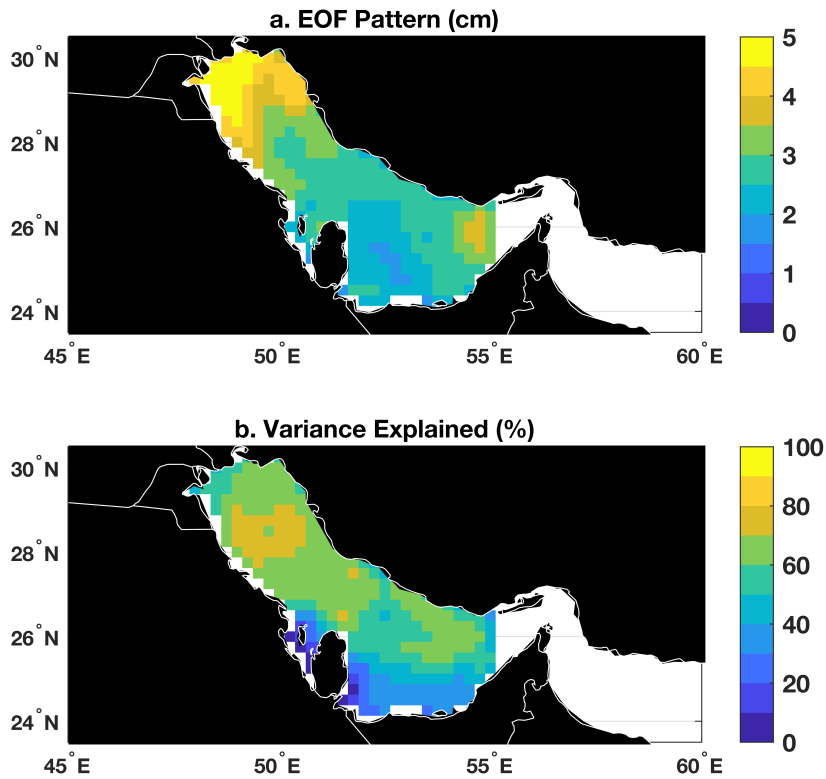
896 **Fig. 9.** Correlation coefficient between Gulf of Oman ζ_0 and altimetric ζ elsewhere over the Indian
 897 Ocean (a.) 1 month earlier or (b.) 2 months earlier (i.e., ζ_0 is lagging ζ elsewhere). Light
 898 shading indicates values that are not distinguishable from zero at the 95% confidence level
 899 (assuming 100 degrees of freedom). 54



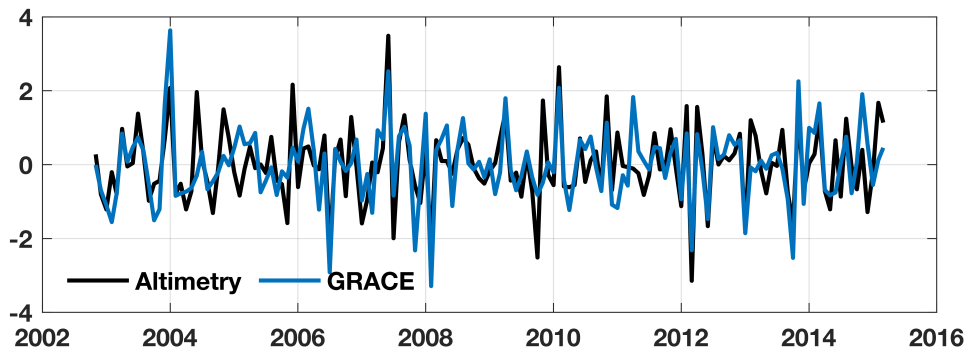
900 FIG. 1. Study area. White lines indicate national boundaries. Color shading identifies ocean depth. (Note the
 901 logarithmic scale bar and units of \log_{10} m.) Red dots denote locations of tide gauges (Table 2). Inset shows the
 902 study area in a global context.



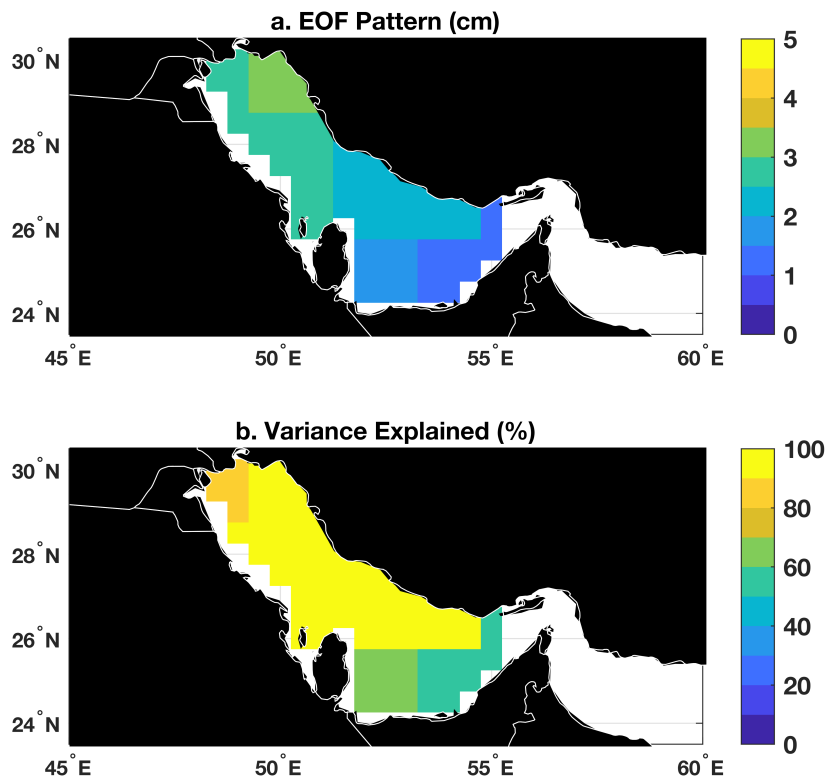
903 FIG. 2. Monthly ocean dynamic sea level in the Persian Gulf between November 2002 and March 2015 from
 904 satellite altimetry (gray, black, blue) and tide gauges (oranges). The satellite-altimetry data are spatially averaged
 905 over the Persian Gulf whereas the tide-gauge data represent a composite average over five sites (Figure 1). The
 906 raw monthly altimetry data are shown in gray, whereas the black and blue indicate the altimetry data with filtering
 907 applied to isolate nonseasonal and intraseasonal timescales, respectively. The tide-gauge data (orange) have been
 908 filtered to isolate intraseasonal periods and adjusted for the inverted-barometer effect. The standard deviations
 909 of the gray, black, blue, and orange time series are 4.7, 3.5, 3.0, and 2.5 cm, respectively.



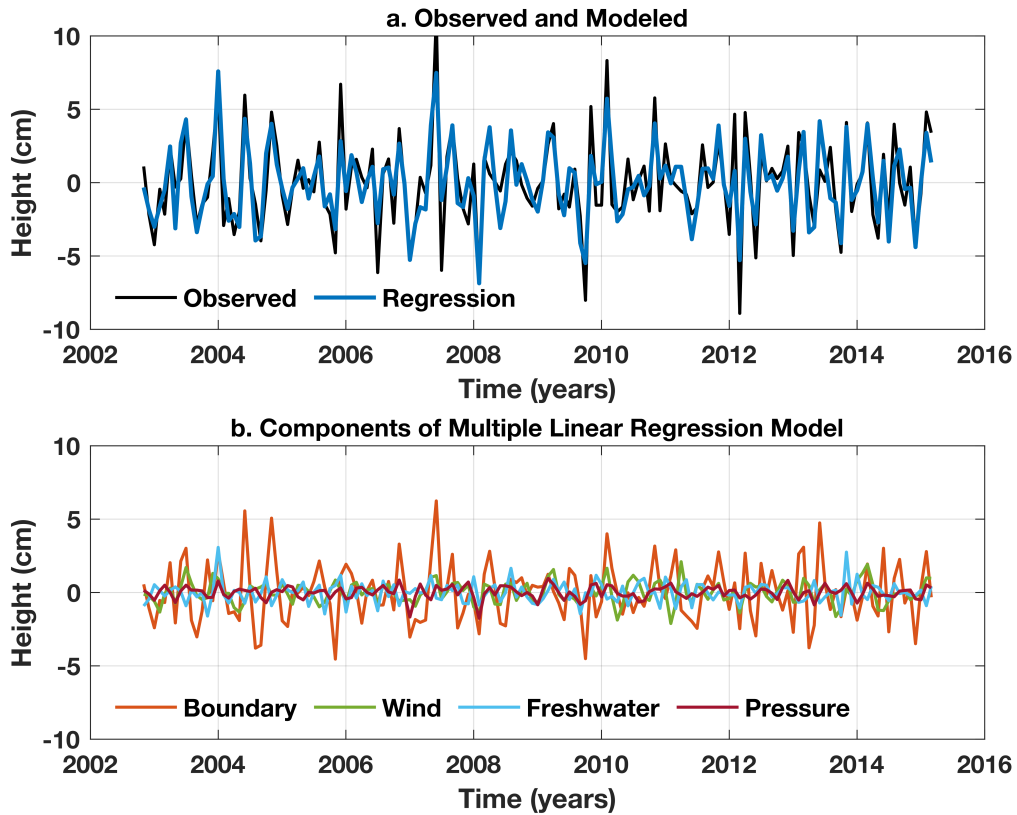
910 FIG. 3. (a.) Spatial pattern (eigenvector) of the first ζ EOF mode across the Persian Gulf from intraseasonal
 911 altimetry data. Units are cm. (b.) Local ζ variance explained by the first EOF mode. Units are percent of total
 912 variance.



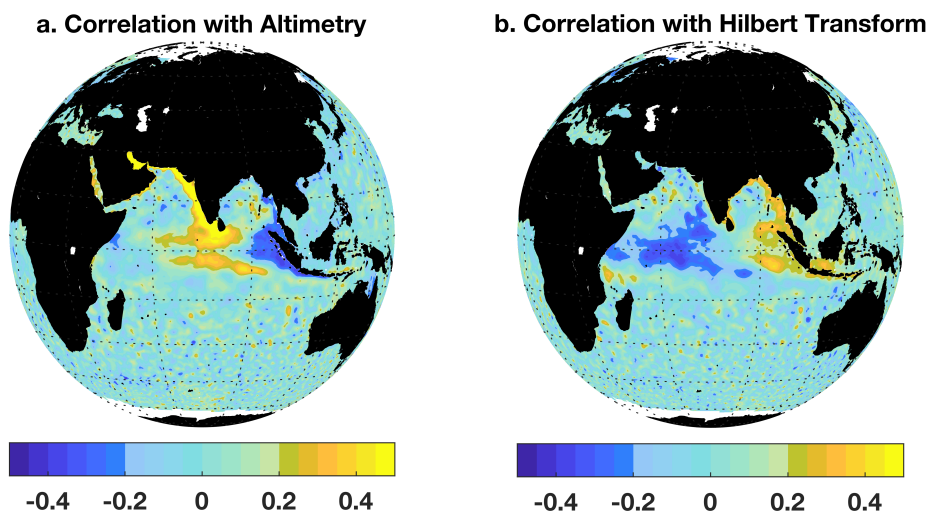
913 FIG. 4. Principal-component time series of the first EOF modes from altimetry ζ (black) and GRACE R_m
 914 (blue) over the Persian Gulf. Time series have been normalized to unit variance (physical units are shown for the
 915 eigenvectors in Figures 3 and 5).



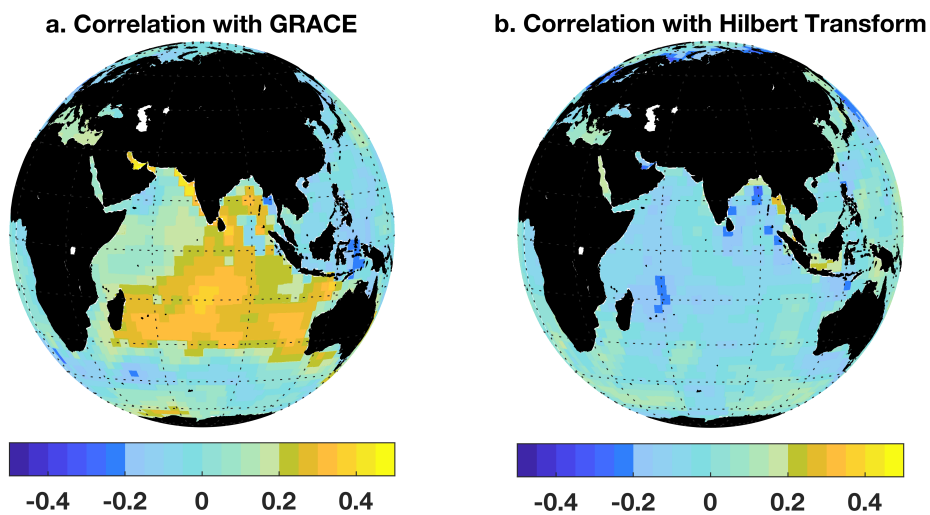
916 FIG. 5. **(a.)** Spatial pattern (eigenvector) of the first R_m EOF mode across the Persian Gulf from intraseasonal
 917 GRACE data. Units are cm. **(b.)** Local R_m variance explained by the first EOF mode. Units are percent of total
 918 variance.



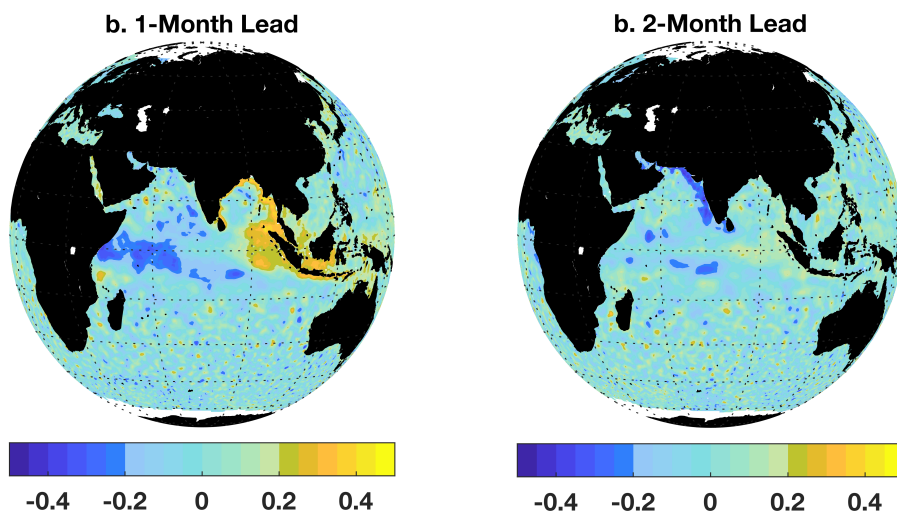
919 FIG. 6. (a.) Time series of intraseasonal $\bar{\zeta}$ from satellite altimetry (black) and the results of the multiple linear
 920 regression model (blue). Units are cm. (b.) Breakdown of contributors to regression model—boundary forcing
 921 ζ_0 (orange), wind stress τ (green), freshwater flux \bar{q} (blue), and barometric pressure \bar{p} (red). Units are cm.



922 FIG. 7. Correlation coefficient between Gulf of Oman ζ_0 and either (a.) ζ from altimetry or (b.) $\mathcal{H}(\zeta)$ over
 923 the Indian Ocean. Light shading indicates values that are not distinguishable from zero at the 95% confidence
 924 level (assuming 100 degrees of freedom).



925 FIG. 8. Correlation coefficient between Gulf of Oman ζ_0 and either (a.) R_m from GRACE or (b.) $\mathcal{H}(R_m)$ over
 926 the Indian Ocean. Light shading indicates values that are not distinguishable from zero at the 95% confidence
 927 level (assuming 100 degrees of freedom).



928 FIG. 9. Correlation coefficient between Gulf of Oman ζ_0 and altimetric ζ elsewhere over the Indian Ocean **(a.)**
 929 1 month earlier or **(b.)** 2 months earlier (i.e., ζ_0 is lagging ζ elsewhere). Light shading indicates values that are
 930 not distinguishable from zero at the 95% confidence level (assuming 100 degrees of freedom).